Mid- and High-Cycle Fatigue of Welded Joints in Steel Marine Structures
Effective Notch Stress and Total Stress Concept Evaluations

Qin, Yanxin; den Besten, Henk; Palkar, Saloni; Kaminski, Miroslaw Lech

DOI
10.1016/j.ijfatigue.2020.105822

Publication date
2021

Document Version
Final published version

Published in
International Journal of Fatigue

Citation (APA)
Qin, Y., den Besten, H., Palkar, S., & Kaminski, M. L. (2021). Mid- and High-Cycle Fatigue of Welded Joints in Steel Marine Structures: Effective Notch Stress and Total Stress Concept Evaluations. *International Journal of Fatigue*, *142*, Article 105822. https://doi.org/10.1016/j.ijfatigue.2020.105822

International Journal of Fatigue 142 (2021) 105822

Contents lists available at ScienceDirect

International Journal of Fatigue

journal homepage: www.elsevier.com/locate/ijfatigue

Mid- and High-Cycle Fatigue of Welded Joints in Steel Marine Structures: Effective Notch Stress and Total Stress Concept Evaluations

Yanxin Qin, Henk den Besten*, Saloni Palkar, Miroslaw Lech Kaminski

Maritime and Transport Technology Department, Delft University of Technology, Delft, the Netherlands

ARTICLE INFO

Keywords:
Steel marine structures
Welded joints
Mid- and high-cycle fatigue
Effective notch stress
Total stress

ABSTRACT

The characteristic far field response spectrum of welded joints – the governing fatigue sensitive locations in steel marine structures – is predominantly linear elastic, meaning mid- and high-cycle fatigue (MCF and HCF) is most important for design. Using the effective notch stress- and the total stress concept, involving respectively S_e and S_T as intact- and cracked geometry fatigue strength criterion, one MCF-HCF resistance curve has been obtained for all welded joints. A generalised random fatigue limit model explicitly incorporating the MCF life time and HCF strength limit scatter provides statistically the most accurate fatigue strength and fatigue life time estimates. Similar MCF performance is obtained for S_e and S_T. Although crack growth dominates the MCF damage process, the results for an initiation related criterion like S_e and natural crack growth related criterion like S_T are similar. Adopting S_e rather than S_T as fatigue strength criterion naturally related to the crack initiation dominated HCF region showing the largest data scatter may explain the better effective notch stress concept HCF performance. Since the HCF resistance scatter is relatively large, the MCF-HCF generalised random fatigue limit model design curves show approximately 1-slope behaviour. meaning that for design purposes a linear Basquin model approximation rather than a piecewise continuous bi-linear MCF-HCF formulation according to guidelines, standards and classification notes should be adopted.

1. Introduction

Renewable energy marine structures like floating offshore wind turbines in deep water (Fig. 1) experience cyclic mechanical loading & response conditions, both environment (wind, waves, current, drifting ice) and service (machinery) induced, meaning fatigue [1] is a governing limit state.

Fatigue sensitive locations in plane geometries turn up at material scale in micro- and meso-scopic stress concentrations (mSC's). In notched geometries, fatigue sensitive locations emerge at structural scale in macro-scopic stress concentrations (MSC's); hot spots (HS's) facilitating mSC's [2], either as part of structural members (e.g. cut-outs) or at structural member connections (e.g. joints). Marine structures are traditionally structural member assemblies in reinforced panel-, truss- or frame-setup and the arc-welded joints typically connecting the structural members are governing in terms of fatigue. Since the structural stiffness distribution is predominantly orthotropic for reinforced panels and member orientation defined for trusses and frames, the uniaxial crack opening mode-I component dominates the welded joint fatigue damage process.

In comparison to shallow water fixed offshore wind turbine support structures, the capital costs of deep water floating ones (Fig. 1) are about twice as high [4]. Deep water typically comes along with an increased distance to shore, meaning wind turbine maintenance costs - including support structure fatigue damage repair - increase as well [5]. Efforts to estimate and improve the fatigue performance of the support structure will increase the engineering and building costs, but provide a good return on investment since maintenance costs will decrease.

Following demonstrator investigations, first commercial use of floating offshore wind turbines is anticipated in between 2020 and 2025 [6]. Design of the envisaged support structures may take advantage of fatigue assessment concepts, relating a fatigue strength criterion S (structural integrity) and the fatigue life time N (structural longevity) using a resistance curve, meant to obtain accurate life time estimates, balanced with criterion complexity and (computational) efforts. Trends have been observed towards the development of complete strength fatigue damage criteria [2]. Incorporating local (notch) information provides more generalised formulations and the number of corresponding fatigue resistance curves reduces accordingly (i.e. ultimately to one), like for the effective notch stress concept [7–13] and the total stress concept [2,3,11].

Fatigue is a cyclic loading & response induced local, progressive,

* Corresponding author.
E-mail address: Henk.denBesten@tudelft.nl (H. den Besten).

https://doi.org/10.1016/j.ijfatigue.2020.105822
Received 12 April 2020; Received in revised form 30 June 2020; Accepted 7 July 2020
Available online 26 July 2020

Nomenclature

Symbols

α	(half) notch angle
β	stress angle
$\boldsymbol{\theta}$	parameter vector
$\chi_{a,s}$	coefficient of (anti-)symmetric $\sigma_n(\cdot)$ part
Δ	prefix indicating stress range
δ	data type (0 = failure, 1 = run-out)
γ	loading & response ratio coefficient
$\lambda_{a,s}$	eigenvalue of (anti-)symmetric $\sigma_n(\cdot)$ part
$\mathscr{L}$	log-likelihood
$\mu_{a,s}$	amplitude of (anti-)symmetric $\sigma_n(\cdot)$ part
ρ	(real) weld notch radius
σ_b	structural bending stress
σ_e	effective notch stress
σ_f	equilibrium equivalent stress part
σ_m	structural membrane stress
$\sigma_n(\cdot)$	weld notch stress distribution
σ_s	(hot spot) structural stress
σ_N	fatigue life time standard deviation
σ_{se}	self-equilibrating stress part
ε	residual
a	crack size
a_i	(real) defect or initial crack size
a_n	(root) notch size
C	fatigue resistance curve intercept
c_l	confidence level
C_{bb}	m_b induced weld load carrying stress coefficient
C_{bm}	f_n induced weld load carrying stress coefficient
C_{bw}	weld load carrying stress coefficient
f_n	line normal force
h_a	attachment height
h_w	weld leg height
k	number of model parameters
$K_I(\cdot)$	weld notch stress intensity distribution
l_a	attachment length
l_w	weld leg length
m	fatigue resistance curve slope
m_b	line bending moment
m_t	slope in HCF region for BB model
m_{bb}	m_b induced weld load carrying bending moment
m_{bm}	f_n induced weld load carrying bending moment
N	number of cycles until failure
n	elastoplasticity coefficient
p_s	probability of survival
r	radial coordinate
r_{lr}	loading & response ratio
r_s	structural bending stress ratio
S	fatigue strength criterion
S_e	effective notch stress range
S_n	nominal stress range
S_s	(hot spot) structural stress range
S_T	total stress range
S_t	MCF-HCF transition strength for BB model
S_∞	fatigue strength limit
$S_{\infty,\mu}$	fatigue strength limit mean value
$S_{\infty,\sigma}$	fatigue strength limit standard deviation
S_y	yield strength
t_b	base plate thickness
t_c	cross plate thickness
t_p	plate thickness
w_s	(specimen) plate width
Y_f	far field factor
Y_n	notch factor
ρ^*	micro- and meso-structural length (or distance)
ρ_f	fictitious notch radius
ρ_{S_∞}	transition curvature parameter for GRFL model
$\hat{}$	circumflex indicating parameter MLE

Abbreviations

AIC	Akaike's information criterion
BB	bi-linear Basquin
BRFL	bi-linear random fatigue limit
CDF	cumulative distribution function
CLB	confidence lower bound
CUB	confidence upper bound
DS	double sided
FE	finite element
GRFL	generalised random fatigue limit
HCF	high-cycle fatigue, $N = O(5\cdot10^6 \sim 10^9)$ cycles
HS	hot spot
LB	linear Basquin
LCF	low-cycle fatigue, $N = O(10^2 \sim 10^4)$ cycles
MCF	mid-cycle fatigue, $N = O(10^4 \sim 5\cdot10^6)$ cycles
MLE	maximum likelihood estimate
mSC	micro- and meso-scopic stress concentration
MSC	macro-scopic stress concentration
ORFL	ordinary random fatigue limit
PDF	probability density function
RFL	random fatigue limit
SS	single sided

structural damage process, turning an intact geometry into a cracked one, meaning elastoplasticity at micro- and meso-material scale as well as macro-structural scale is involved. The amount of elastoplasticity: large, medium or small, is affecting the damage process as reflected in the corresponding characteristic low-, mid- and high-cycle fatigue (LCF, MCF and HCF) regions of the resistance curves. Note that in other research disciplines the LCF, MCF and HCF regions are referred to as low, high and very high cycle fatigue regions [14] or even low, high and giga cycle fatigue regions [15]. A characteristic far field response spectrum of welded joints in steel marine structures like floating offshore wind turbines is predominantly linear elastic, explaining why S is typically of the stress type and particularly related to MCF and HCF.

The MCF performance of welded joints HS type C has already been investigated using the effective notch stress concept and total stress concept, involving respectively an intact and cracked geometry based fatigue strength criterion [11]. Only complete data (i.e. failures) have been considered. Adopting different MCF-HCF fatigue resistance curve formulations (Section 2), the effective notch stress concept and total stress concept performance for welded joint HS's type C, B and A will be investigated (Section 3), taking advantage of explicit weld notch stress (intensity) distribution formulations. Both complete and right-censored data (i.e. failures and run-outs) will be incorporated.

2. Mid- and high-cycle fatigue

For MCF and HCF typically a log–log linear $N(S)$ dependency is observed (Fig. 2) and a 3-parameter $\{\log(C), m, \sigma_N\}$ 1-slope formulation, the semi-empirical Basquin (LB) model, is naturally adopted:

$$log(N) = \log(C) - m\cdot\log(S). \quad (1)$$

Intercept $\log(C)$, slope m and standard deviation σ_N are respectively the endurance, damage mechanism and fatigue life time scatter parameters. Shifting from MCF to HCF, the slope m is typically increasing, implying a change in fatigue damage mechanism, i.e. from crack growth governing to crack initiation dominated. Intercept $\log(C)$ decreases accordingly. At the same time it is observed that the number of crack nucleation sites reduces [15–17], meaning that the life time scatter parameter σ_N increases.

MCF-HCF modelling requires a 2-slope formulation. Following a description of characteristic fatigue physics (Section 2.1), suitable MCF-HCF models will be explored (Section 2.2). Being able to deal with both complete and right-censored data, the Maximum Likelihood approach [3,18] will be used to obtain model parameters and quantile estimates (Section 2.3).

2.1. Physics in materials and structures

The elastoplasticity requirement to develop fatigue damage (Section 1) suggests the existence of a barrier, a fatigue strength limit S_∞. For $(S < S_\infty)$ the fatigue life time will be infinite $(N \to \infty)$.

At material level, elastoplasticity turns up at mSC's. Instantly, mSC's emerge at the boundaries of the anisotropic polycrystalline grain structure (source 1) and at inclusions/voids/pores (source 2). Over time, moving dislocations concentrate in (persistent) slip bands introducing intrusion-extrusion pairs (source 3) induced mSC's because of the material surface roughening. For large and medium amounts of elastoplasticity, fatigue cracks typically develop first at the governing intrusion-extrusion pair (source 3) induced mSC at/near the surface, since the response condition changes from plane stress at/near the surface to plane strain in subsurface material. For small amounts of elastoplasticity cracks may still develop. In case of a face centred cubic material structure typically at/near the surface at the grain boundary (source 1) or at inclusion/void/pore (source 2) induced mSC's. For a body centred cubic material structure cracks typically develop subsurface first, since mSC's at subsurface (non-metallic) inclusions/voids/pores (source 2) are in charge [19,20]. For smaller amounts of elastoplasticity a fatigue strength limit most likely exists [19].

At structural level, elastoplasticity emerges at MSC's. The arc-welding process introduces a notch, an MSC, at the weld toe and depending on the penetration level another one at the weld root, as well as additional mSC's: surface defects and sub-surface inclusions/voids/pores (source 4). For large, medium as well as small amounts of (notch) elastoplasticity, fatigue cracks develop at/near the structure surface of the MSC location [14,17,21,22]. A material contribution can be involved [23,24]. For smaller amounts of elastoplasticity a fatigue strength limit may exist.

Fig. 1. Floating offshore wind turbines with a support structure in spar-buoy (left), semi-submersible (middle) and tension leg platform (right) configuration [6].

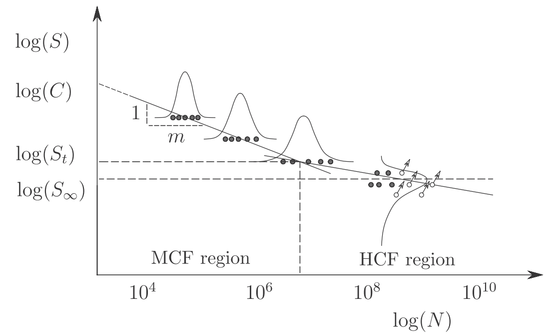

Fig. 2. MCF and HCF fatigue resistance characteristics.

2.2. Model formulations

In case a finite slope in both the MCF and HCF region is observed, a bi-linear Basquin (BB) model can be adopted. Although typically a piecewise continuous one is used [25–27] in guidelines (e.g. IIW), standards (e.g. Eurocode 3) and classification notes (e.g. DNV-GL), a continuous 5-parameter $\{\log(C), m, S_t, m_t, \sigma_N\}$ formulation may be preferred in order to include a gradual MCF-HCF transition:

$$\log(N) = \log(C) - m\cdot\log(S) - \left\{\left(\frac{m}{m_t}\right) - 1\right\}\cdot \log[1 + \exp\{\log(S) - \log(S_t)\}^{-m_t}]. \tag{2}$$

For $(S > S_t)$ the MCF slope m is in charge; for $(S < S_t)$ the HCF slope m_t (Fig. 2). However, σ_N contains both the MCF and HCF life time scatter contribution, meaning that the MCF region description suffers from the increased HCF scatter.

In case the HCF slope tends to become infinite $(m_t \to \infty)$, typically random rather than constant fatigue strength limit behaviour is introduced: $(N \to \infty)$ for $(S < S_\infty(\mu, \sigma))$, reflecting the stochastic nature of the mSC size, location, number and orientation, as well as the random MSC size. Assuming that in the MCF and HCF region, respectively, the fatigue life time and the fatigue strength scatter are governing, the BB model (Eq. 2) turns into a 5-parameter $\{\log(C), m, S_{\infty,\mu}, S_{\infty,\sigma}, \sigma_N\}$ ordinary random fatigue limit (ORFL) model [28]:

$$\log(N) = \log(C) - m\cdot\log\{S - S_\infty(\mu, \sigma)\}. \tag{3}$$

Alternatively a 5-parameter $\{\log(C), m, S_{\infty,\mu}, S_{\infty,\sigma}, \sigma_N\}$ piecewise-continuous bi-linear random fatigue limit (BRFL) model can be adopted [29], providing a better alignment with the guidelines, standards and classification notes:

$$\log(N) = \log(C) - \frac{m\cdot\log(S)}{H\{S - S_\infty(\mu, \sigma)\}}. \tag{4}$$

The Heaviside Step Function $H()$ reflects the piecewise-continuous MCF-HCF transition. For both the ORFL and BRFL model the transition behaviour is fixed. Introducing a transition curvature parameter $\rho_{S\infty}$, a 6-parameter $\{\log(C), m, \sigma_N, S_{\infty,\mu}, S_{\infty,\sigma}, \rho_{S\infty}\}$ generalised random fatigue limit (GRFL) model can be obtained [30]:

$$\log(N) = \log(C) - m\cdot\log(S) - \rho_{S\infty}\cdot\log\left\{1 - \frac{S_\infty(\mu, \sigma)}{S}\right\}. \tag{5}$$

For $\rho_{S\infty} \to m$ the GRFL model turns into the ORFL one. If the data does not contain fatigue limit behaviour, the LB model appears: $\rho_{S\infty} \to 0$.

A high finite or (near) infinite HCF slope value provides the opportunity to apply either a BB or one of the random fatigue limit (RFL) models. Because of the cyclic plasticity requirement to develop fatigue damage, a fatigue strength limit may exist. However, considering the multiple mSC sources as well as the random nature of both the mSC and MSC size, the cyclic plasticity requirement might be identically satisfied for any loading & response level [31], meaning fatigue strength limit behaviour may not be observed. In particular for welded joints in marine structures, since additional environment induced mSC's like corrosion pits (source 5) may appear over time. The size of existing mSC's may increase and new ones may develop, accelerating the fatigue damage process.

Fatigue strength limit behaviour will remain a hypothesis anyway and difficult to prove. Theoretically, the number of cycles N required to obtain fatigue damage can always be increased. At the same 'time' the available HCF data is limited because of (testing) time constraints and the HCF slope estimate, either finite or (near) infinite, is sensitive to the data involved. However, from engineering perspective it is ultimately all about accurate fatigue strength and life time estimates, meaning that an accurate MCF-HCF transition is important. Let regression analysis show if either a BB or a RFL model provides (statistically) the best performance.

2.3. Parameter and quantile estimates

The MCF-HCF models (Eqs. 2–5) relate the independent variable, predictor $\log(S)$, to the dependent one, response $\log(N)$. Regression analysis can be adopted to estimate the model parameters. Although the Least Squares approach minimising the sum of the (log)Normal distributed residuals squared $\varepsilon \sim N(0,1)$ is popular, MCF-HCF fatigue resistance data sets typically cannot be dealt with properly since both complete and right-censored data, failures and run-outs, are involved. Using the Maximum Likelihood approach [3,18] the data joint probability density is maximised and the most likely parameter vector $\hat{\theta}$ estimate can be obtained:

$$\max_{\theta}\{\mathcal{L}(\theta;N|S)\} \tag{6}$$

with log-likelihood

$$\mathcal{L}(\theta;N|S) = \sum_{j=1}^{n} \delta_j \cdot \log\{f(N_j|S_j;\theta)\} + (1-\delta_j)\cdot\log\{1 - F(N_j|S_j;\theta)\}$$

and

$$\delta_j = \begin{Bmatrix} 0 & \text{for a failure} \\ 1 & \text{for a run}-\text{out} \end{Bmatrix}.$$

A probability density function (PDF) $f(x;\mu,\sigma)$ and corresponding cumulative distribution function (CDF) $F(x;\mu,\sigma)$ assumption is required. In case of a Basquin model for the fatigue life time, the (log)Normal PDF and CDF can be adopted based on probabilistic arguments and empirical success:

$$\begin{aligned} f_N(x;\mu,\sigma) &= \frac{1}{\sqrt{2\pi}\cdot\sigma}\cdot\exp\left[-\frac{\{\log(x)-\mu\}^2}{2\sigma^2}\right] \\ F_N(x;\mu,\sigma) &= \frac{1}{2}\left[1+\operatorname{erf}\left\{\frac{\log(x)-\mu}{2\sigma}\right\}\right]. \end{aligned} \tag{7}$$

Although $f_N(x;\mu,\sigma)$ and $F_N(x;\mu,\sigma)$ are quite flexible and the log-scale data satisfies the physical fatigue life time lower bound ($\log(N=1) = 0$), the failure rate (f_N/F_N) shows non-monotonic behaviour. Monotonically increasing behaviour would be expected, since early failures are excluded for MCF-HCF. The (log)Weibull extreme value distribution $W(x;\mu,\sigma)$ might be a solution since the failure rate is monotonically increasing by definition, while maintaining the lower bound requirement and flexibility:

$$\begin{aligned} f_W(x;\mu,\sigma) &= \left(\frac{1}{\sigma}\right)\cdot\exp\left[\frac{\{\log(x)-\mu\}}{\sigma} - \exp\left[\frac{\{\log(x)-\mu\}}{\sigma}\right]\right] \\ F_W(x;\mu,\sigma) &= 1-\exp\left[-\exp\left[\frac{\{\log(x)-\mu\}}{\sigma}\right]\right]. \end{aligned} \tag{8}$$

The mean value and standard deviation of the fatigue life time and/or fatigue strength limit (log)Normal PDF and CDF regression analysis induced residual $\varepsilon \sim N(0,1)$ are respectively $\mu(\varepsilon)=0$ and $\sigma(\varepsilon)=1$. However, the (log)Weibull PDF and CDF $\varepsilon \sim W(0,1)$ reflects the 63^{rd} percentile with $\mu(\varepsilon) = -\gamma$ (Euler constant) and $\sigma(\varepsilon) = \pi/\sqrt{6}$. In order to have a competitive unbiased model [32], the location and scale parameters $\{\mu,\sigma\}$ have to be modified:

$$\begin{aligned} f_W(x;\mu,\sigma) &\to f_W\left(x;\mu+\gamma\cdot\frac{\sqrt{6}}{\pi}\cdot\sigma,\ \frac{\sqrt{6}}{\pi}\cdot\sigma\right) \\ F_W(x;\mu,\sigma) &\to F_W\left(x;\mu+\gamma\cdot\frac{\sqrt{6}}{\pi}\cdot\sigma,\ \frac{\sqrt{6}}{\pi}\cdot\sigma\right). \end{aligned} \tag{9}$$

A sample size bias correction could be incorporated as well for both the (log)Normal and (log)Weibull PDF and CDF, but is considered not to be necessary since the fatigue resistance data sample size is sufficiently large (Section 3).

For the LB (Eq. 1) and BB (Eq. 2) model with respectively $\theta = \{\log(C), m, \sigma_N\}$ and $\theta = \{\log(C), m, S_t, m_t, \sigma_N\}$, the fatigue life time PDF $f(N|S;\mu_N,\sigma_N)$ and CDF $F(N|S;\mu_N,\sigma_N)$ involve the same scale parameter σ_N. However, the location parameter is different:

$$\begin{Bmatrix} \mu_{N_{LB}} = \log(C) - m\cdot\log(S) \\ \mu_{N_{BB}} = \log(C) - m\cdot\log(S) - \left\{\left(\frac{m}{m_t}\right)-1\right\}\cdot \\ \log[1+\exp\{\log(S)-\log(S_t)\}^{-m_t}] \end{Bmatrix}. \tag{10}$$

The ORFL and BRFL model with $\theta = \{\log(C), m, S_{\infty,\mu}, S_{\infty,\sigma}, \sigma_N\}$ as well as the GRFL model with $\theta = \{\log(C), m, S_{\infty,\mu}, S_{\infty,\sigma}, \rho_{S\infty}, \sigma_N\}$ require both a fatigue life time and fatigue limit PDF and CDF assumption. Adopting either the (log)Normal or (log)Weibull PDF and CDF (respectively Eq. 7 and 8), the marginal (joined) fatigue life time PDF and CDF become:

$$\begin{aligned} f_{RFL}(N|S;\mu_N,\sigma_N) &= \int_{-\infty}^{S} f(N|S;\mu_N,\sigma_N)\cdot f(x;\mu_{S_\infty},\sigma_{S_\infty})\mathrm{d}x \\ F_{RFL}(N|S;\mu_N,\sigma_N) &= \int_{-\infty}^{S} F(N|S;\mu_N,\sigma_N)\cdot f(x;\mu_{S_\infty},\sigma_{S_\infty})\mathrm{d}x \end{aligned} \tag{11}$$

with

$$\begin{Bmatrix} \mu_{N_{ORFL}} = \log(C) - m\cdot\log(S-x) \\ \mu_{N_{BRFL}} = \log(C) - \frac{m\cdot\log(S)}{H(S-x)} \\ \mu_{N_{GRFL}} = \log(C) - m\cdot\log(S) - \rho_{S_\infty}\cdot\log(1-\frac{x}{S}) \end{Bmatrix}. \tag{12}$$

Partitioning $\theta = \{\theta_1,\theta_2\}$, the relative parameter profile log-likelihood can be obtained for θ_1 (e.g. $\log(C)$):

$$\mathcal{L}_r(\theta_1) = \max_{\theta_2}\left\{\frac{\mathcal{L}(\theta_1,\theta_2;N|S)}{\mathcal{L}(\hat{\theta};N|S)}\right\}. \tag{13}$$

A more likely value is obtained for $\mathcal{L}_r(\theta_1)\to 1$; a less likely one for $\mathcal{L}_r(\theta_1)\to 0$. Since the inverse of the parameter log-likelihood squared $-2\cdot\mathcal{L}_r(\theta_1)$ is asymptotically chi-squared distributed [28], a likelihood ratio test can be adopted to estimate the two-sided parameter confidence interval for confidence level $c_l = (1-\eta)$:

$$-2\cdot\mathcal{L}_r(\theta_1) \leqslant \chi^2_{1;1-\eta}. \tag{14}$$

Evaluating the regression analysis results for different $\{f, F\}$ assumptions, the best fit is obtained for the smallest $\mathcal{L}(\hat{\theta};N|S)$ reflecting the largest joint probability density, provided the number of model parameters k is the same. However, if k differs from one model to another, Akaike's Information Criterion (AIC) can be adopted [33], since more model parameters means generally speaking a better fit. The smaller AIC, the better:

$$\mathrm{AIC} = -2\{\mathcal{L}(\hat{\theta};N|S) - k\}. \tag{15}$$

The S-N fatigue resistance quantile for design at a required reliability (i.e. probability of survival p_s) and confidence level c_l, $R(p_s)C(c_l)$, can be established using:

$$F(N|S;\hat{\theta}) = F(N|S;\hat{\mu}_N,\hat{\sigma}_{N,cl}) = (1-p_s). \tag{16}$$

Only for the LB and BB models (Eq. 1 and 2) an explicit *S-N* quantile formulation can be obtained:

$$F(N|S;\hat{\mu}_N, \hat{\sigma}_{N,cl}) = F\left(\frac{\log(N) - \hat{\mu}_N(S)}{\hat{\sigma}_{N,cl}}\right) = (1 - p_s),$$

meaning

$$\log(N) = \hat{\mu}_N(S) + F^{-1}(1 - p_s)\cdot\hat{\sigma}_{N,cl}. \tag{17}$$

Note that the *S-N* quantiles (Eq. 16 and 17) are based on curve wise rather than point wise confidence [3,11], incorporating respectively the global and local data scatter. In case the fatigue resistance data sample size is sufficiently large (i.e. assuming confidence is sufficiently large), typically the R(0.977) quantile $\log(N) = \hat{\mu}_N(S) - 2\cdot\hat{\sigma}_N$ is adopted, assuming the fatigue life time is (log)Normal distributed [34]. For smaller data sample size a R(0.95) C(0.75) *S-N* quantile is adopted in order to achieve a similar reliability level as obtained for a sufficiently large data sample size. The C(0.75) corresponds to a probability of failure $(1 - p_s) = 10^{-4}$ in the last year of a 20-years marine structure fatigue design life time [35,36].

3. Mid- and high-cycle fatigue of welded joints

Macroscopic stress concentrations, HS's, in arc-welded joints emerge at the weld notch locations. Different types are distinguished (Fig. 3) and have been classified as [37,38]:

- HS type C: weld toe notch along the weld seam at the plate surface
- HS type B: weld toe notch at the weld seam end at the plate edge
- HS type A: weld toe notch at the weld seam end at the plate surface.

The HS structural stress concept is commonly applied in engineering [2,25–27]. Using a shell/plate finite element (FE) model, typically a (non-)linear surface extrapolation based HS structural stress range $S_s = \Delta\sigma_s$ estimate is obtained, although quite sensitive to FE type and mesh size [37].

Considering a through-thickness crack as an appropriate fatigue design criterion, force and moment equilibrium based linear interior interpolation can be used to calculate exact S_s values [39,40]. Involving a relatively coarse meshed shell/plate FE model is typically sufficient. The local weld geometry is not included, meaning that corresponding notch information is missing. However, the (linear) predominant mode-I fatigue damage related far field stress distribution in each cross-section along the weld seam is available. Transforming the nodal normal forces $F_{n,i}$ and bending moments $M_{b,i}$ for HS's type C (Fig. 4 top) along the weld seam to line forces and moments f_n and m_b, $\{F_n\} = [T]\cdot\{f_n\}$ and $\{M_b\} = [T]\cdot\{m_b\}$ [40], the membrane and bending structural stress components $\sigma_m = (f_n/t_p)$ and $\sigma_b = (6\cdot m_b/t_p^2)$ can be calculated to obtain $\sigma_s = (\sigma_m + \sigma_b)$. For weld end HS's type B a virtual $t_p{}'$ rather than a real plate thickness t_p is involved (Fig. 4 middle), meaning $\sigma_m = \Sigma F_{n,i}/(t_p\cdot t_p{}')$ and $\sigma_b = \{\Sigma(F_{n,i}\cdot x_i) - \sigma_m\cdot t_p{}'^2/2\}/(t_p\cdot t_p{}'^2)$. The coordinate system origin should be at the HS location to minimise mesh size sensitivity [3]. Since the local weld geometry is not included, for weld end HS's type A a virtual node [40] can be introduced (Fig. 4 bottom). Using force and moment equilibrium the nodal normal forces $\{F_{n1}, F_{n2}\}$ and bending moments $\{M_{b1}, M_{b2}\}$ of the element next to the weld end are redistributed over its length l_e, assuming that the line normal force f_n and bending moment m_b are constant over the weld end length l_{we} and decreases linearly over $(l_e - l_{we})$. Using the line force $f_n = \{F_{n1}\cdot(l_{we} + l_e) + F_{n2}\cdot(l_{we} - l_e)\}/(l_{we}\cdot l_e)$ and line moment $m_b = \{M_{b1}\cdot(l_{we} + l_e) + M_{b2}\cdot(l_{we} - l_e)\}/(l_{we}\cdot l_e)$, $\sigma_s = (\sigma_m + \sigma_b) = (f_n/t_p) + (6\cdot m_b/t_p^2)$ like for HS's type C.

Different fatigue assessment concepts have been developed over time aiming to obtain more accurate life time estimates, balanced with criterion complexity and (computational) efforts [2,41–44]. The involved fatigue strength criteria have evolved from global to local ones and tend to become more generalised formulations, reducing the number of corresponding resistance curves ultimately to one, like for the effective notch stress concept [7–13] and the total stress concept [2,3,11].

The through-thickness (crack) weld notch stress distribution $\sigma_n(r/t_p)$ typically contains three zones: the zone 1 peak stress, the zone 2 notch-affected stress gradient and the zone 3 far field dominated stress gradient [3,11]. Whereas an intact geometry fatigue strength criterion like the HS structural stress σ_s contains only equilibrium equivalent stress related zone 3 far field content, the effective notch stress already includes partial zone 1, 2 and 3 information.

However, fatigue scaling requires the zone 1 peak stress value as well as the zone 2 notch affected- and zone 3 far field dominated gradient to be incorporated, meaning a fatigue strength criterion should take the complete distribution into account. For the effective (i.e. average) notch stress, a nominal stress value would be obtained. The stress intensity factor K_I seems to meet the complete distribution criterion and the intact geometry related notch stress distribution has been translated into a cracked geometry equivalent in order to obtain the total stress fatigue strength criterion.

Exploiting the σ_s related semi-analytical weld notch stress (intensity) formulations (Section 3.1 and 3.2) for welded joint HS's type C, B and A, MCF-HCF resistance data from literature (Section 3.3) will be used to investigate the effective notch stress concept (Section 3.4) and total stress concept (Section 3.5) performance in terms of Akaike's information criterion AIC and the parameter confidence.

3.1. Weld notch stress distributions

Semi-analytical $\sigma_n(r/t_p)$ formulations have already been derived, exploiting (non-) symmetry conditions with respect to $(t_p/2)$, assuming $\sigma_n(r/t_p)$ is a linear superposition of an equilibrium equivalent part σ_f (i.e. the linear structural field stress) and a self-equilibrating stress part σ_{se} (consisting of a V-shaped notch stress component [45,46] and a weld load carrying stress component). For a weld toe notch, $\sigma_n(r/t_p)$ denotes in case of non-symmetry [3,11]:

$$\begin{aligned}\sigma_n\left(\frac{r}{t_p}\right) = \sigma_s\Bigg\{&\left(\frac{r}{t_p}\right)^{\lambda_s-1}\mu_s\lambda_s(\lambda_s+1)[\cos\{(\lambda_s+1)\beta\}-\\&\qquad\chi_s\cos\{(\lambda_s-1)\beta\}]+\\&\left(\frac{r}{t_p}\right)^{\lambda_a-1}\mu_a\lambda_a(\lambda_a+1)[\sin\{(\lambda_a+1)\beta\}-\\&\qquad\chi_a\sin\{(\lambda_a-1)\beta\}]+\\&C_{bw}\cdot\left\{2\left(\frac{r}{t_p}\right)-1\right\}-2\cdot r_s\cdot\left(\frac{r}{t_p}\right)\Bigg\}\end{aligned} \tag{18}$$

and in case of symmetry [3,11]:

$$\begin{aligned}\sigma_n\left(\frac{r}{t_p}\right) = \sigma_s\Bigg\{&\left[1-2r_s\left\{1-f\left(\frac{r}{t_p}=\frac{1}{2}\right)\right\}\right]f\left(\frac{r}{t_p}\right)+\\&r_s\left\{2f\left(\frac{r}{t_p}=\frac{1}{2}\right)-1\right\}\cdot\left[f\left(\frac{r}{t_p}\right)+\left\{1-f\left(\frac{r}{t_p}=\frac{1}{2}\right)\right\}-2\left(\frac{r}{t_p}\right)\right]\Bigg\}\end{aligned} \tag{19}$$

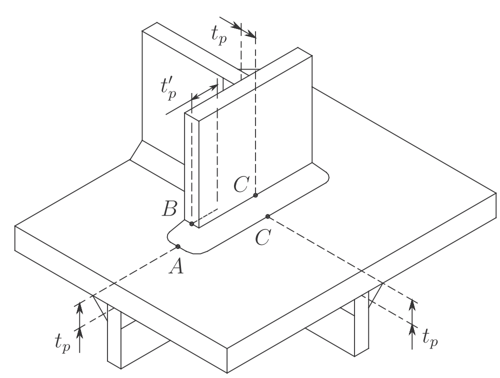

Fig. 3. HS type C, B and A classification [37].

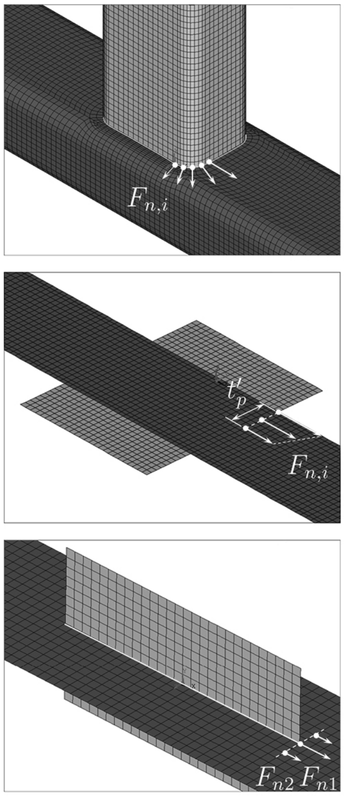

Fig. 4. Typical shell/plate FE models for welded joints HS type C (top), B (middle) and A (bottom).

with

$$f\left(\frac{r}{t_p}\right) = \sigma_s \left\{\left(\frac{r}{t_p}\right)^{\lambda_s - 1} \mu_s \lambda_s (\lambda_s + 1)[\cos\{(\lambda_s + 1)\beta\} - \chi_s \cos\{(\lambda_s - 1)\beta\}] + \left(\frac{r}{t_p}\right)^{\lambda_a - 1} \mu_a \lambda_a (\lambda_a + 1)[\sin\{(\lambda_a + 1)\beta\} - \chi_a \sin\{(\lambda_a - 1)\beta\}] + C_{bw} \cdot \left\{4\left(\frac{r}{t_p}\right) - 1\right\} - 2 \cdot r_s \cdot \left(\frac{r}{t_p}\right)\right\}$$

and

$$f\left(\frac{r}{t_p} = \frac{1}{2}\right) = \frac{(\lambda_a - \lambda_s)(\lambda_a \lambda_s - 2C_{bw})}{\lambda_a(\lambda_a - 1) - \lambda_s(\lambda_s - 1)} + C_{bw}.$$

Plane strain conditions have been assumed, meaning 3D effects [47] can be neglected [42]. For HS's type C and A at the base plate $t_p = t_b$ and at the connecting/cross/cover plate $t_p = t_c$. An artificial plate thickness $t_p = t_p'$ is introduced for HS's type B. Coefficients μ_s and μ_a are obtained using force and moment equilibrium. The involved eigenvalues λ_s and λ_a, the eigenvalue coefficients χ_s and χ_a as well as the stress angle $\beta = (\alpha - \pi/2)$ are notch angle α dependent. The structural stress $\sigma_s = (\sigma_m + \sigma_b)$ and the structural bending stress ratio $r_s = (\sigma_b/\sigma_s)$ are the FE analysis obtained far field stress parameters [3,11].

The weld geometry causes a local change in stiffness; a shift in neutral axis, meaning the weld becomes load carrying up to some extent. Considering a weld toe notch as typically encountered in a welded joint without symmetry with respect to $(t_p/2)$, a counter-clockwise bending moment is introduced for a normal line force f_n pointing to the right and a clockwise bending line moment m_b. The corresponding weld load carrying (bending) stress distribution particularly affects the zone 2 stress gradient (Eq. 18). For a weld toe notch of a welded joint showing symmetry with respect to $(t_p/2)$ the same principle applies to the related half plate thickness.

The weld load carrying stress component is geometry $(t_b, t_c, l_w, h_w, a_n)$ and loading (f_n, m_b) dependent, meaning coefficient C_{bw} contains the notch stress distribution specific information. With respect to loading, $\sigma_s C_{bw}$ is assumed to be linear superposition of a normal force and bending moment induced structural field membrane stress and bending stress component:

$$\sigma_s C_{bw} = \sigma_m C_{bm} + \sigma_b C_{bb} \tag{20}$$

meaning

$$C_{bm} = \frac{m_{bm}}{\sigma_s(1 - r_s)} \cdot \left(\frac{6}{t_p^2}\right)$$

and

$$C_{bb} = \frac{m_{bb}}{\sigma_s r_s} \cdot \left(\frac{6}{t_p^2}\right).$$

Bending moments m_{bm} and m_{bb} are estimated using a FE beam model in order to obtain weld load carrying stress information, uncoupled from V-shaped notch behaviour. Alternatively, a C_{bw} estimate is obtained using a parametric function, fitted with input from FE notch stress distributions for a range of geometry dimensions and loading parameter values.

Double weld element beam models for HS's type C in T-joints and cruciform joints have been developed [11], replacing the original single weld element beam models [3]. Investigating the C_{bw} requirements for HS's type B as typically observed in in-plane (Fig. 4 middle) and out-of-plane gusset plate joints, respectively the double sided (DS) T-joint and double sided cruciform joint formulations proved to be sufficient for the cases showing respectively non-symmetry and symmetry with respect to $(t_p'/2)$. For HS's type A like typically observed at the weld ends of attachments or brackets (Fig. 4 right), a cover plate joint double weld element beam model (Fig. 6) turned out to be much more effective than the single weld element configuration (Fig. 5) to obtain the local C_{bw}. Global attachment and bracket induced effects are captured in σ_s.

As a first step in the beam model verification, for 2 load cases: a normal force f_n and bending moment m_b, the relative base plate load path contribution has been compared to results obtained using a FE solid model for reference (Figs. 7 and 8). The considered range of dimensions is representative for marine structures consisting of thin plate/shell structural members. Beam model application is not limited to the absolute geometry dimensions as shown (Figs. 7 and 8), but the range for particular relative ones, (l_w/t_b) and (h_w/l_w) has to be satisfied.

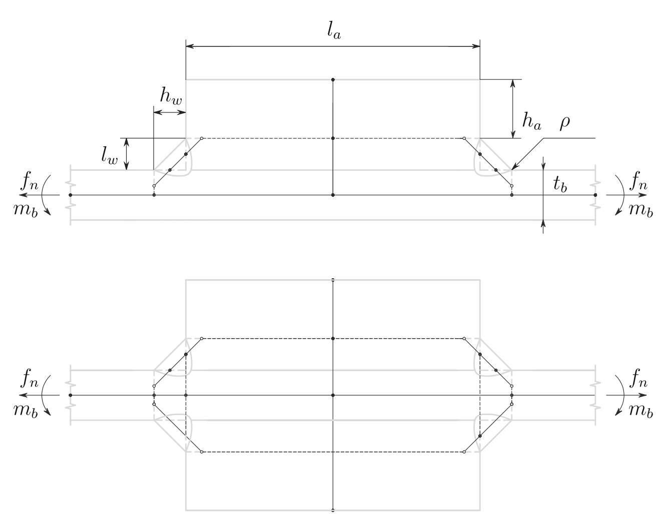

Fig. 5. SS (top) and DS (bottom) cover plate joint single weld element beam model for non-symmetry and symmetry with respect to $(t_p/2)$.

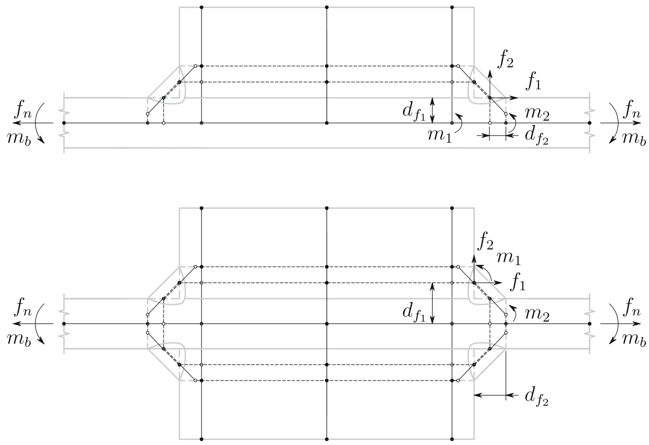

Fig. 6. SS (top) and DS (bottom) cover plate joint double weld element beam model for non-symmetry and symmetry with respect to $(t_p/2)$.

If loading is applied to the base plate, the single sided (SS) cover plate contains 2 parallel load paths: 1 through the base plate and 1 through the weld and cover plate. The normal stiffness and bending stiffness of the load paths define how the loading is divided. Applying a normal force f_n to the base plate, the base plate load path related normal stiffness dominates generally speaking the weld and cross plate load path related bending stiffness, explaining the $(f_{n,t_b}/t_b)$ values closer to 1 (Fig. 7a–d). The bending stiffness is involved for both load paths if a bending moment m_b is applied. Because of the relatively large l_a, the cover plate attracts a significant part of the load as reflected in the relatively small $(m_{b,t_b}/t_b)$ values (Fig. 7e–h); i.e. the weld is relatively more load carrying. For the DS cover plate, 3 parallel load paths are involved: 1 through the base plate and 2 through the weld and cover plates, meaning the normal forces (Fig. 8a–d and bending moments (Fig. 8e–h) through the base plate will be smaller in comparison to the SS cover plate values (Fig. 7) because of the relatively smaller stiffness contribution of each load path. The trends for f_n and m_b are the same. For increasing t_b, the normal force and bending moment through the base plate are increasing because of increasing base plate load path stiffness. The weld and cover plate load path bending stiffness is increasing for increasing l_a, l_w and h_w, meaning the base plate load path contribution is slightly decreasing. For h_w variations (Figs. 7 and 8) the wrong trend for the single weld element beam models can be observed.

Second step is to correlate the beam model nodal moments and forces to m_{bm} and m_{bb}. For the f_n load case, internal bending moments are introduced and the ones showing the same trend as the required C_{bm} (obtained fitting FE solid model weld notch stress distributions and the semi-analytical formulation, Eq. 18 and 19) for varying joint dimensions, m_1 and m_2 (Fig. 6), can be related to m_{bm}. Assuming that except m_1 and m_2 in the weld toe cross-section (the physical part) a coefficient to match the FE and semi-analytical solutions (the fitting part) is involved as well, the m_{bm} estimate yields for the SS cover plate:

$$m_{bm} = \left(\frac{1}{13}\right)\cdot(m_1 + m_2). \tag{21}$$

For the m_b load case, internal normal forces are introduced and f_1 and f_2 (Fig. 6) show the same trend as the required C_{bb}. Involving respectively d_{f_1} and d_{f_2} to complete the physical part related bending moment and adding the fitting part, the m_{bb} estimate becomes for the SS cover plate:

$$m_{bb} = (f_1\cdot d_{f_1} + f_2\cdot d_{f_2}). \tag{22}$$

For the DS cover plate similar results are obtained:

$$m_{bm} = \left(\frac{7}{2}\right)\cdot(m_1 + m_2) \tag{23}$$

and

$$m_{bb} = \left(\frac{2}{15}\right)\cdot(f_1\cdot d_{f_1} + f_2\cdot d_{f_2}). \tag{24}$$

Comparing for the SS cover plate the required C_{bm} and C_{bb} values to the estimates (Fig. 9a–d), good results are obtained. Depending on the joint dimensions, the weld load carrying stress level for the base plate weld toe notch can be up to 30 [%] of the structural stress σ_s. On the other hand, for DS cover plates the weld load carrying stress level does not even reach 10 [%] of σ_s (Fig. 9e–h).

Although for varying t_b and l_a the load distribution over the base plate and cover plate may change, C_{bw} is hardly affected (Fig. 9a, b, e, f). In fact, the weld dimensions l_w and h_w typically define C_{bw} (Fig. 9c, d, g, h), since asymptotic $C_{bw}(t_b, l_a)$ behaviour is obtained for $l_a \gg t_b$. In case $l_a \to t_b$, the cover plate tends to behave like a cross-plate and C_{bw} becomes t_b and l_a sensitive, like observed for the DS T-joint and DS cruciform joint [11].

Alternative to a beam model based weld load carrying stress estimate, involving a physical and fitting part, a parametric fitting function has been obtained as well. For the SS cover plate:

$$\begin{aligned} C_{bm} &= -0.187\cdot e^{-0.527\cdot W} + 0.209 \\ C_{bb} &= -0.271\cdot e^{-0.889\cdot W} + 0.302 \end{aligned} \tag{25}$$

and for the DS cover plate:

$$\begin{aligned} C_{bm} &= -0.056\cdot e^{-0.760\cdot W} + 0.079 \\ C_{bb} &= -0.045\cdot e^{-0.370\cdot W} + 0.076 \end{aligned} \tag{26}$$

with

$$W = \left(\frac{h_w}{l_w}\right).$$

The parametric fitting functions involve an exponential term reflecting a notch angle contribution as well as a polynomial one representing the log-ratio of the 2 involved load path parameters.

Third and last step is to investigate the weld toe notch stress distributions for different loading combinations. For illustration purposes monotonic through-thickness weld toe notch stress distributions of a SS cover plate are shown (Fig. 10a, b) for a pure bending moment ($r_s = 1$) and combined load case ($r_s = 1/3$); the bending moment is applied clockwise. Non-monotonic ones are shown for a pure normal force ($r_s = 0$) and a different combined load case ($r_s = -1$) with counter-clockwise bending moment (Fig. 10c, d). The adopted joint dimensions are arbitrary but reflect at the same time results for cases with almost the largest difference between C_{bw} fit and beam values (Fig. 9).

Monotonic through-thickness weld toe notch stress distributions $\sigma_n(r/t_p)$ of a DS cover plate for the far field load cases ($r_s = 1$) and ($r_s = 1/3$) are shown (Fig. 10e, f) as well as non-monotonic ones (Fig. 10g, h); ($r_s = 0$) and ($r_s = -1$). Observation shows that for $0 < (r/t_p) < (1/2)$ equilibrium is satisfied as imposed. For $(1/2) < (r/t_p) < 1$, the self-equilibrating stress part definition is lost since the weld notch contribution is not taken into account. The (anti-) symmetry condition ensures a stress gradient close to r_s.

Converged FE solid model solutions are added for comparison, showing that the semi-analytical $\sigma_n(r/t_b)$ formulations (Eq. 18 and 19) provide accurate weld notch stress distributions.

Although for HS's type B the weld load carrying coefficients C_{bw} are

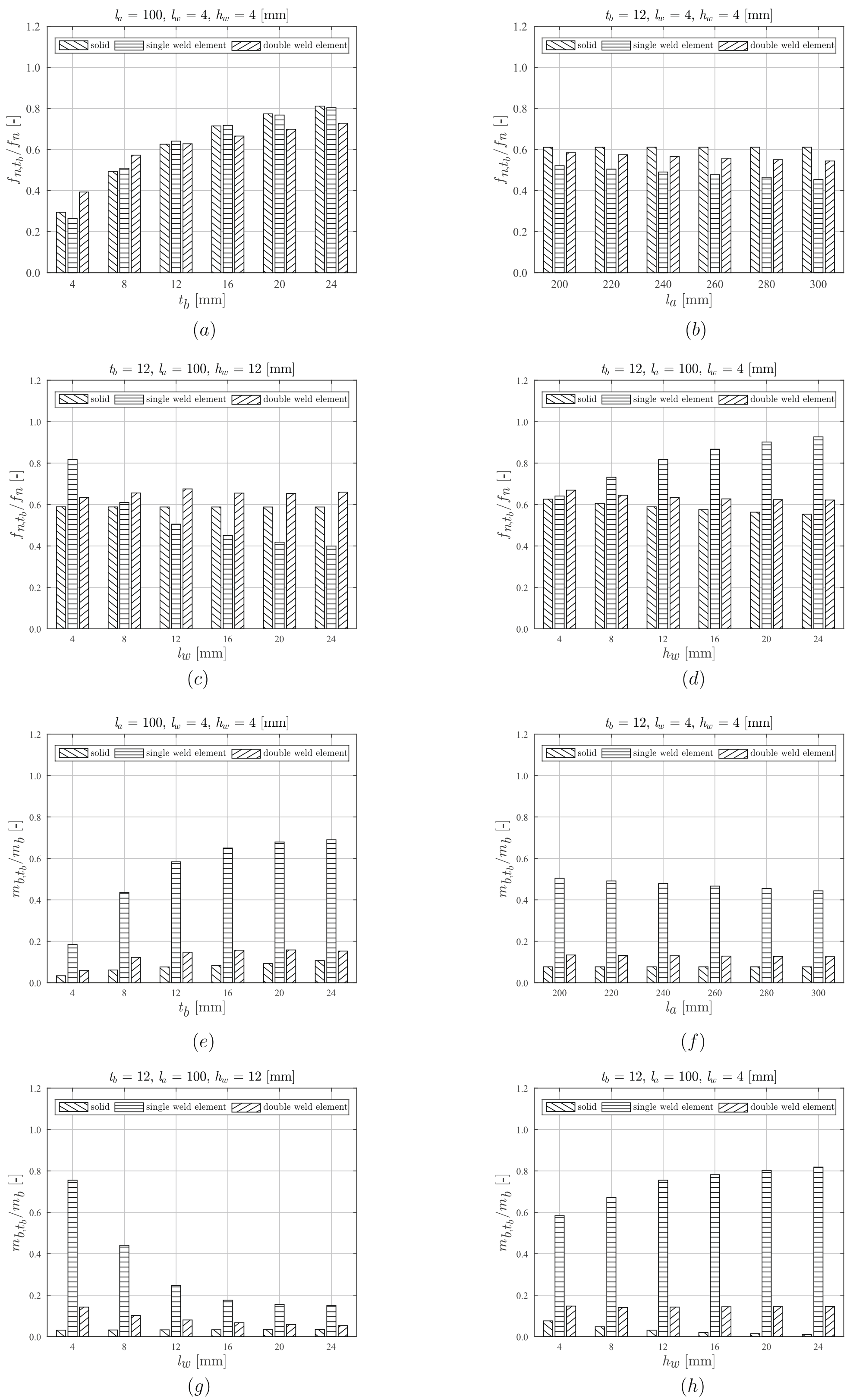

Fig. 7. SS cover plate relative base plate load for varying t_b, l_w and h_w for applied normal force (a–d) and bending moment (e–h).

similar to (non-symmetric) T-joint and (symmetric) cruciform joint based estimates, question remains what t_p' value should be adopted for typical in-plane and out-of-plane gusset plate joints (Fig. 14d–f). Comparing semi-analytical weld notch stress distributions to FE results (1 [MPa] nominal membrane stress is applied) for a range of t_p' values, good agreement is obtained for the non-symmetry cases (Fig. 11a, c). For the symmetry cases the best results are obtained for $t_p' = 20...40$ [mm], since the symmetry condition at $(t_p'/2)$ compromises the results up to some extent (Fig. 11b, d). At the same, the notch affected zone size turns out to be ~ 4 [mm] no matter the plate width value w_s,

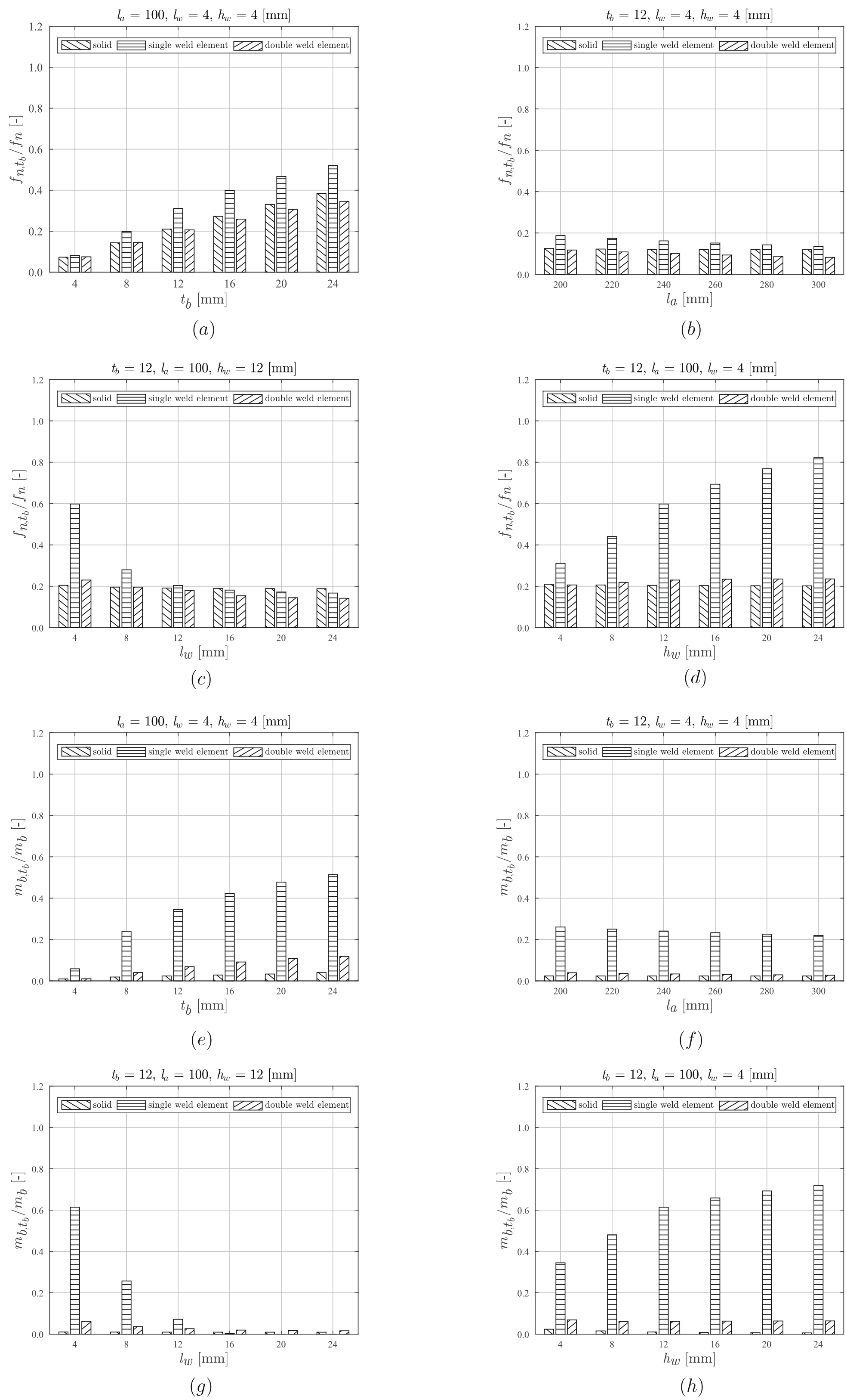

Fig. 8. DS cover plate relative base plate load for varying t_b, l_w , h_w and a_n for applied normal force (a–d) and bending moment (e–h).

explaining why a characteristic $t_p{}'$ value is proposed. Since the notch affected zone size for typical HS's type C and A is about 10 to 20 [%] of the plate thickness, i.e. $0.1t_p...0.2t_p$, $t_p{}' = 20...40$ [mm] seems to be reasonable. A most likely value will be established using regression analysis, aiming to capture the $t_p{}'$ providing the most accurate fatigue life time estimate (Section 3.4).

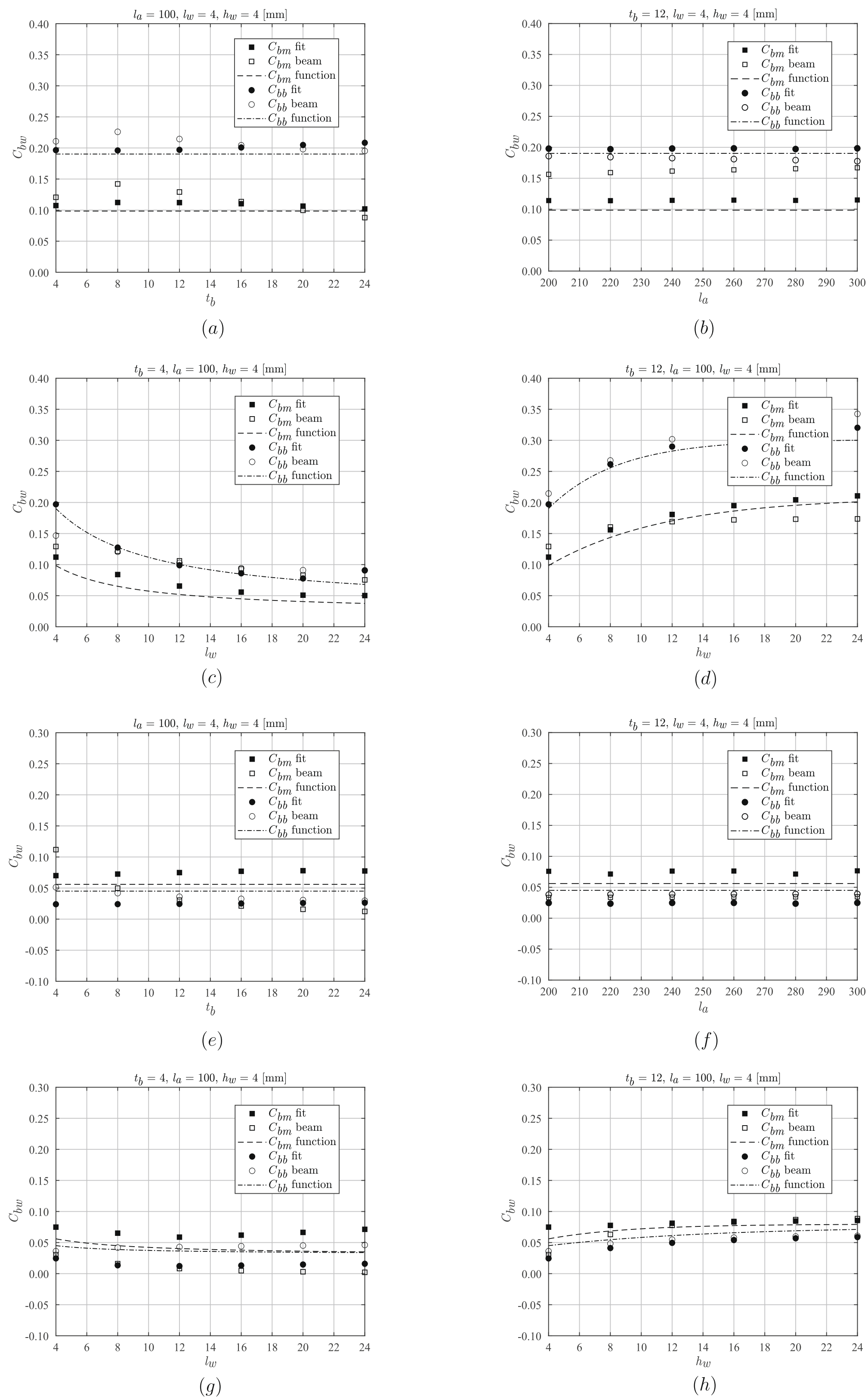

Fig. 9. SS (a–d) and DS (e–h) cover plate C_{bm} and C_{bb} fit as well as beam model estimate for varying t_b, l_a, l_w and h_w.

3.2. Weld notch stress intensity distributions

Consistently using the equilibrium equivalent and self-equilibrating parts of the intact geometry related mode-I weld toe notch stress distributions (Eqs. 18 and 19), the corresponding cracked geometry related weld toe notch stress intensity distributions $K_I(a/t_p)$ include a crack size-dependent far field and notch factor [3]:

$$K_I\left(\frac{a}{t_p}\right) = \sigma_s\sqrt{t_p}\cdot Y_n\left(\frac{a}{t_p}\right)\cdot Y_f\left(\frac{a}{t_p}\right)\cdot\sqrt{\pi\left(\frac{a}{t_p}\right)}. \tag{27}$$

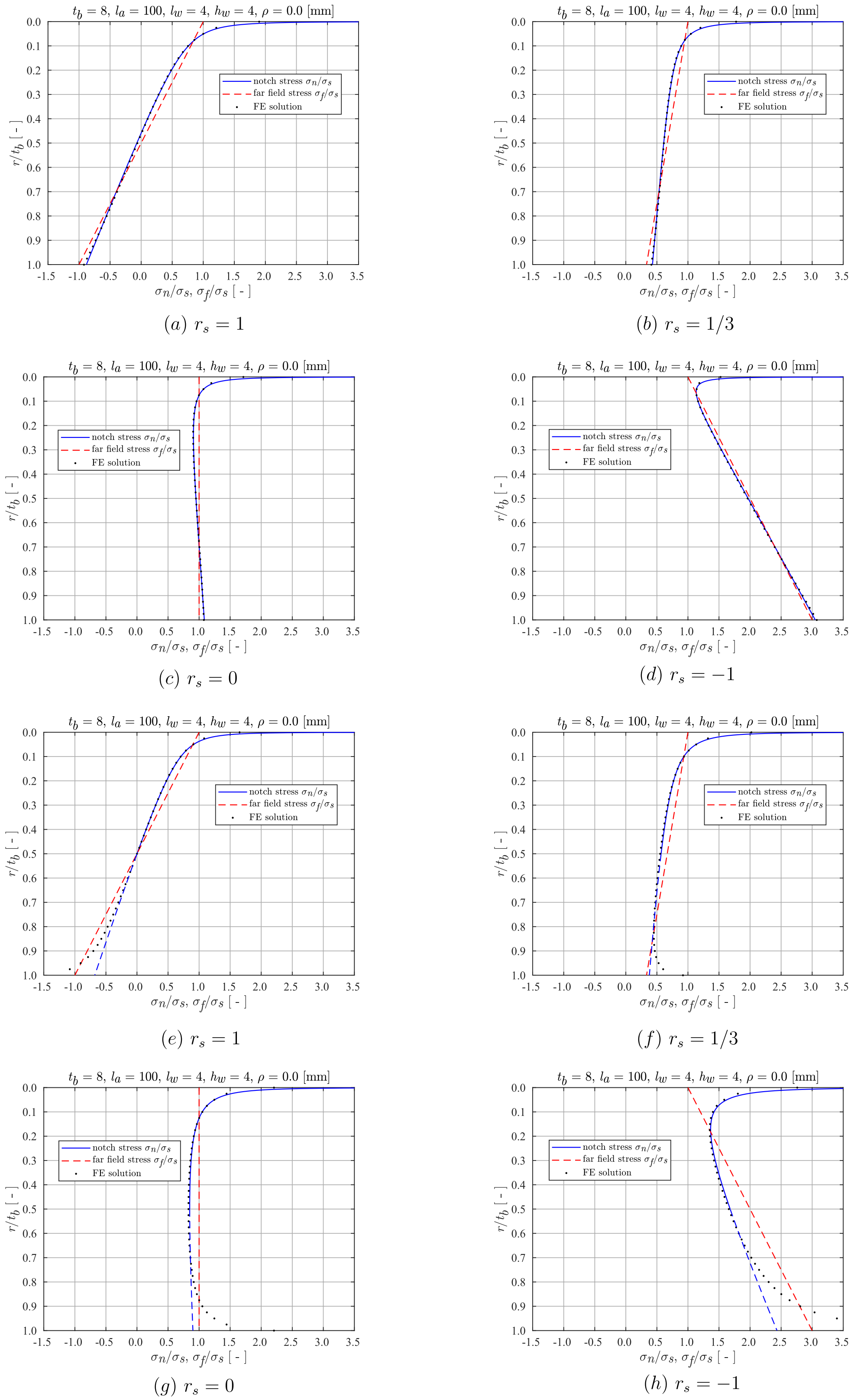

Fig. 10. SS (a–d) and DS (e–h) cover plate weld toe notch stress distributions.

For HS's type C and A, either $t_p = t_b$ or $t_p = t_c$; for HS's type B, $t_p = t_p{'}$. Far-field factor Y_f contains the zone 3 associated equilibrium equivalent (membrane and bending) stress contributions as well as the crack related geometry effects like finite plane dimensions and free surface behaviour. For weld toe notches showing either non-symmetry or symmetry with respect to $(t_p/2)$, a single-edge crack formulation is adopted. In case of symmetry one notch is assumed to be governing. Handbook solutions are available [48]. Notch factor Y_n incorporates the zones 1 and 2 governing self-equilibrium equivalent stress contribution, applied as crack face traction. For the non-symmetry case:

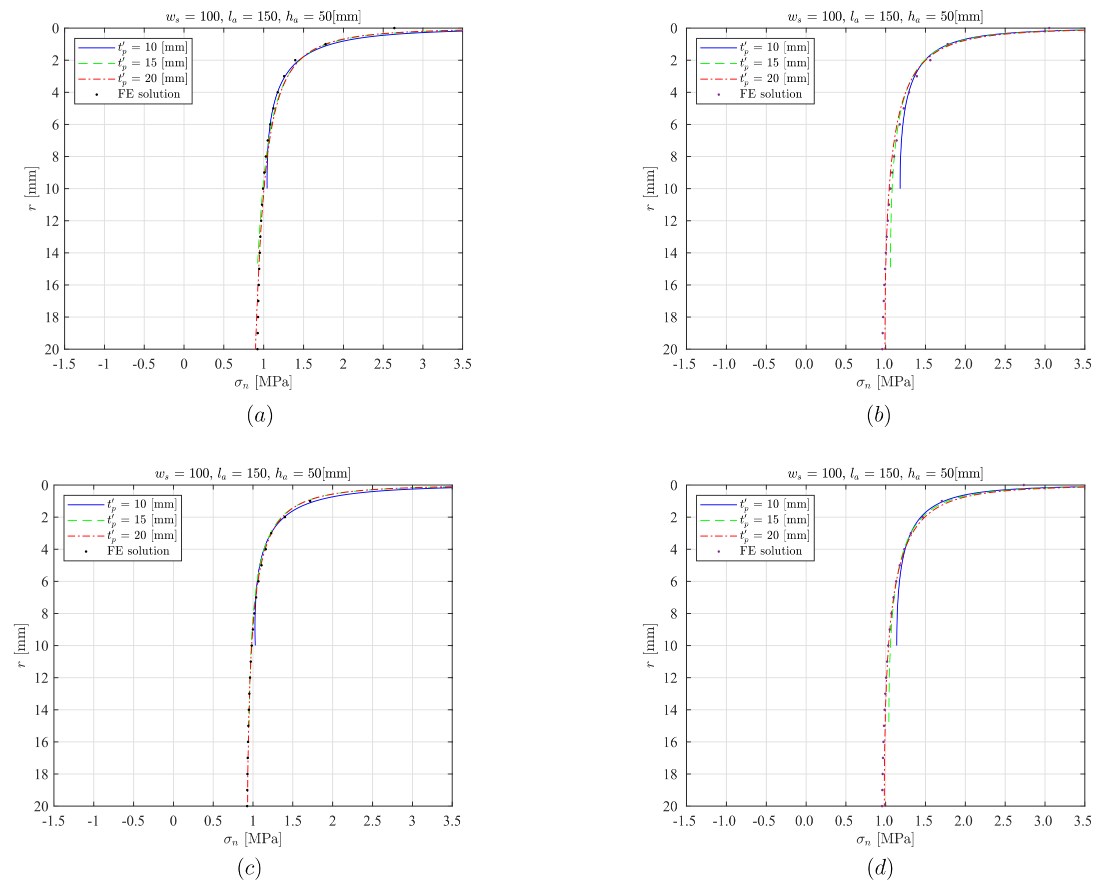

Fig. 11. SS and DS in-plane gusset plate (a–b) as well as SS and DS out-of-plane gusset plate (c–d) weld notch stress distributions.

$$Y_n\left(\frac{a}{t_p}\right) = \left(\frac{2}{\pi}\right)\Bigg[\left(\frac{a}{t_p}\right)^{\lambda_s-1}\mu_s\left(\frac{\sqrt{\pi}}{2}\right)\frac{\Gamma\left(\frac{\lambda_s}{2}\right)}{\Gamma\left(\frac{\lambda_s+1}{2}\right)}\lambda_s(\lambda_s+1)\cdot [\cos\{(\lambda_s+1)\beta\} - \chi_s\cos\{(\lambda_s-1)\beta\}] + \left(\frac{a}{t_p}\right)^{\lambda_a-1}\mu_a\left(\frac{\sqrt{\pi}}{2}\right)\frac{\Gamma\left(\frac{\lambda_a}{2}\right)}{\Gamma\left(\frac{\lambda_a+1}{2}\right)}\lambda_a(\lambda_a+1)\cdot [\sin\{(\lambda_a+1)\beta\} - \chi_a\sin\{(\lambda_a-1)\beta\}] + C_{bw}\left\{2\left(\frac{a}{t_p}\right) - \frac{\pi}{2}\right\}\Bigg] \tag{28}$$

and for the symmetry case:

$$Y_n\left(\frac{a}{t_p}\right) = \left(\frac{2}{\pi}\right)\left(\left[1 - 2r_s\left\{1 - f\left(\frac{a}{t_p} = \frac{1}{2}\right)\right\}\right] f\left(\frac{a}{t_p}\right) + r_s\left\{2f\left(\frac{a}{t_p} = \frac{1}{2}\right) - 1\right\}\left[\left\{1 - f\left(\frac{a}{t_p} = \frac{1}{2}\right)\right\}\left(\frac{\pi}{2}\right) - 2\left(\frac{a}{t_p}\right)\right] + 2r_s\left(\frac{a}{t_p}\right)\right) \tag{29}$$

with

$$f\left(\frac{a}{t_p}\right) = \left(\frac{a}{t_p}\right)^{\lambda_s-1}\mu_s\left(\frac{\sqrt{\pi}}{2}\right)\frac{\Gamma\left(\frac{\lambda_s}{2}\right)}{\Gamma\left(\frac{\lambda_s+1}{2}\right)}\lambda_s(\lambda_s+1) [\cos\{(\lambda_s+1)\beta\} - \chi_s\cos\{(\lambda_s-1)\beta\}] + \left(\frac{a}{t_p}\right)^{\lambda_a-1}\mu_a\left(\frac{\sqrt{\pi}}{2}\right)\frac{\Gamma\left(\frac{\lambda_a}{2}\right)}{\Gamma\left(\frac{\lambda_a+1}{2}\right)}\lambda_a(\lambda_a+1)\cdot [\sin\{(\lambda_a+1)\beta\} - \chi_a\sin\{(\lambda_a-1)\beta\}] + C_{bw}\left\{4\left(\frac{a}{t_p}\right) - \frac{\pi}{2}\right\}.$$

With respect to the weld toe notch stress distributions (Eqs. 18 and 19) through-thickness crack coordinate (a/t_p) naturally replaced through-thickness stress coordinate (r/t_p). The SS and DS cover plate weld toe notch stress intensities $Y_n Y_f$ for the far-field load cases (Fig. 10) are shown for illustration purposes (Fig. 12). Notch factor Y_n turns out to be governing for $\{0 < (a/t_p) \leqslant 0.2\}$; a zone 1 and 2 weld geometry stress (concentration) affected micro-crack region. Far-field factor Y_f rules the zone 3 far-field stress related macro-crack region $\{0.2 < (a/t_p) \leqslant 1\}$. The $Y_n Y_f$ estimates are in good agreement with FE solid model solutions. Note that the involved C_{bw} values contain almost the largest difference between fit and beam values (Figs. 9 and 12).

3.3. Fatigue resistance data

Multiple arc-welded joint constant amplitude fatigue resistance data series available in literature (Figs. 13 and 14, Table 1) have been re-investigated. The data series reflect several characteristic welded joint features, including HS type (C, B and A), (non-)symmetry with respect to $(t_p/2)$ and weld type (groove and fillet). All steel small scale specimens are in as-welded condition. The sample size is ~ 1900.

The base plate thickness t_b ranges from 2 to 160 [mm], specimen plate width w_s from 4 to 210 [mm], the loading & response ratio r_{rl} from −1.0 to 0.8 [–] and the yield strength S_y from 245 to 1030 [MPa]. The applied load is either a (3- or 4-point) bending moment or a normal force. Fatigue life times N cover the MCF and HCF region; i.e. $N = O(10^4 \ldots 10^9)$ cycles.

Aim is to obtain a balanced contribution of welded joint characteristics, although the cover plate joint and gusset plate joint are somewhat under represented (Table 1).

3.4. Effective notch stress concept

The fatigue life time of welded joints consists of an initiation (i.e.

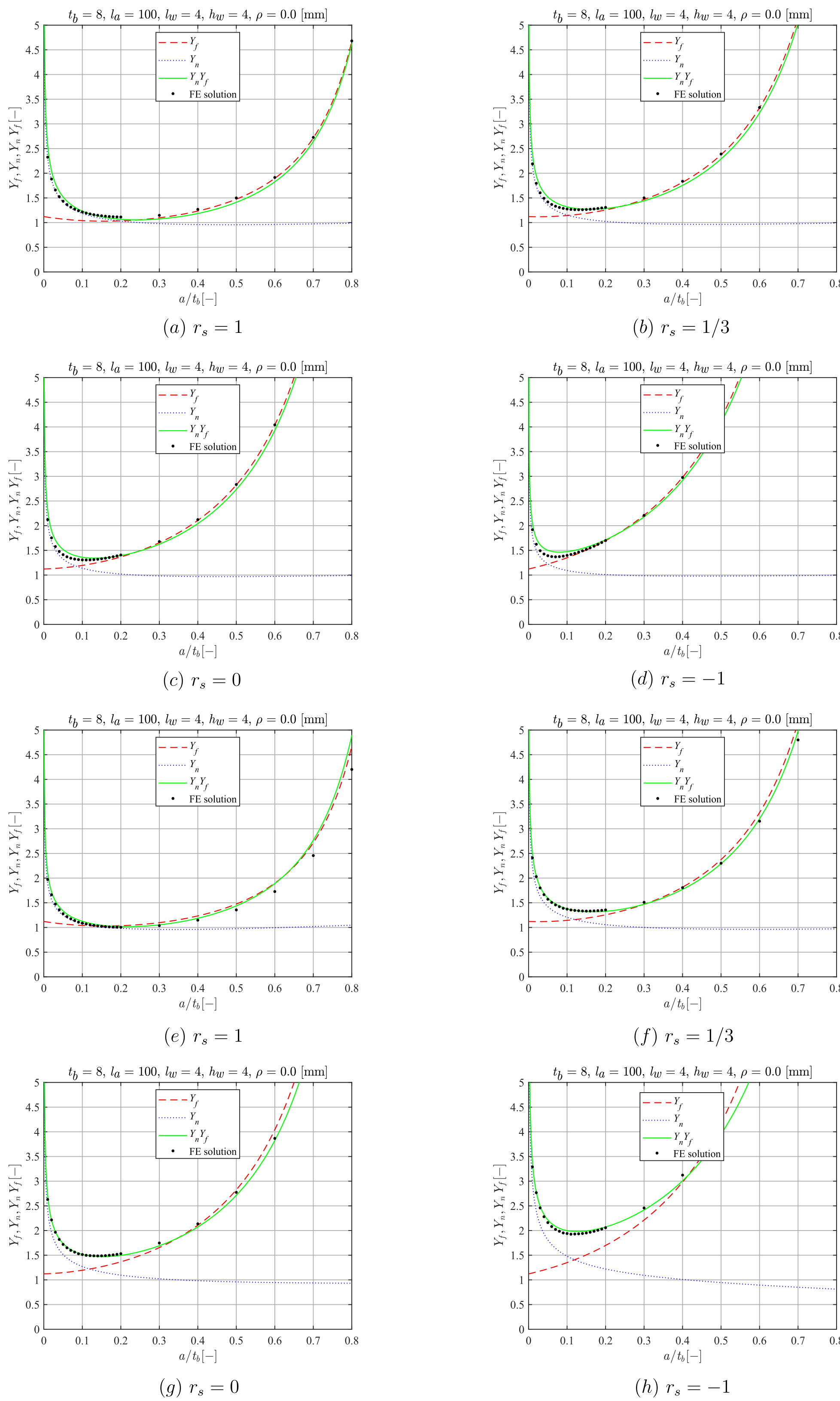

Fig. 12. SS (a–d) and DS (e–h) cover plate base plate weld toe notch stress intensity distributions.

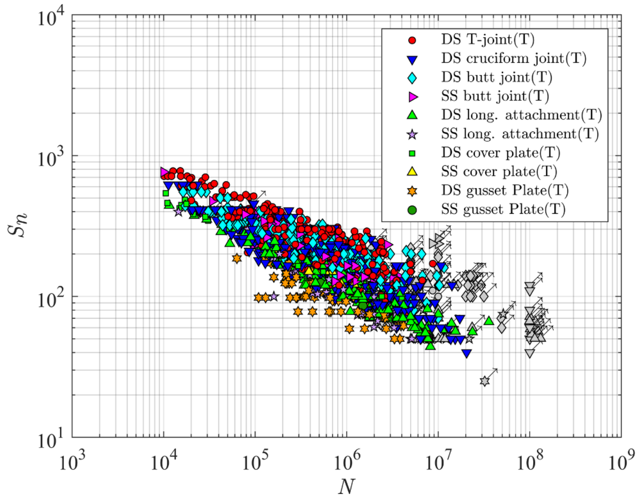

Fig. 13. Nominal stress based MCF-HCF fatigue resistance data.

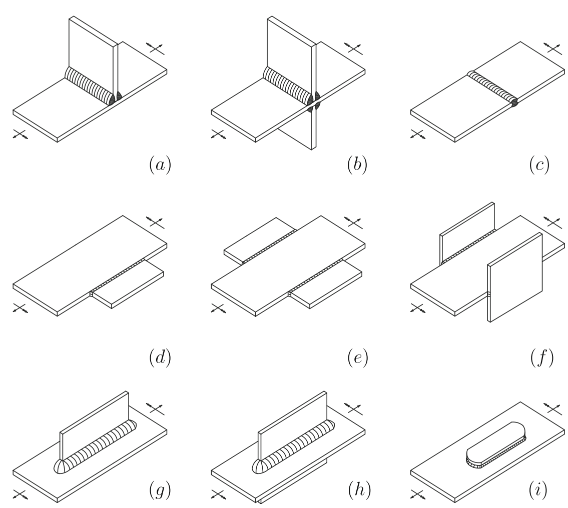

Fig. 14. Hot spot type C (a–c), B (d–f) and A (g–i) small scale specimens.

Table 1
Welded joint fatigue resistance data.

Joint type	HS type	Weld type	Sample size
DS T-joint [49–60]	C	fillet	~ 330
DS cruciform joint [61–63,50,64–72]	C	fillet	~ 400
SS butt joint [73–75]	C	groove	~ 120
DS butt joint [76–84,55]	C	groove	~ 410
SS cover plate joint[85]	C	fillet	~ 30
DS cover plate joint [86,87,50,88]	C	fillet	~ 50
SS gusset plate joint [89]	B	fillet	~ 10
DS gusset plate joint [90–92,89,93,87]	B	fillet	~ 80
SS long. attachment [60,94–96,88]	A	fillet	~ 100
DS long. attachment [97–116]	A	fillet	~ 270

micro-crack growth) and (macro-crack) growth contribution. If the major part is initiation related, an intact geometry based fatigue strength criterion seems justified. However, the (as) weld(ed) notch radius ρ is typically small and a zone 1 peak stress criterion would be too conservative. Adopting a micro- and meso-structural notch support hypothesis, an effective notch stress range estimate $S_e = \Delta\sigma_e$ can be obtained by averaging the notch stress distribution along the (presumed) crack path over a material characteristic micro- and meso-structural length or distance ρ^*, partially incorporating a zone 2 notch stress gradient- and zone 3 far field stress gradient contribution as well [7,9,8,10,11]. Typically, a solid FE solution is required to estimate S_e. However, taking advantage of the weld notch stress distribution formulations (Eqs. (18) and (19)), intact geometry fatigue strength criterion $S_e = \Delta\sigma_e$ includes for weld toe notches in case of non-symmetry:

$$\begin{aligned}\sigma_e &= \frac{1}{\rho^*}\int_0^{\rho^*} \sigma_n(r)\mathrm{d}r\\ &= \sigma_s\cdot\left(\frac{t_p}{\rho^*}\right)\cdot\left\{\left(\left(\frac{\rho^*}{t_p}\right)^{\lambda_s}\mu_s(\lambda_s+1)[\cos\{(\lambda_s+1)\beta\}-\right.\right.\\ &\chi_s\cos\{(\lambda_s-1)\beta\}]+\\ &\left(\frac{\rho^*}{t_p}\right)^{\lambda_a}\mu_a(\lambda_a+1)[\sin\{(\lambda_a+1)\beta\}-\\ &\chi_a\sin\{(\lambda_a-1)\beta\}]+\\ &\left.C_{bw}\cdot\left\{\left(\frac{\rho^*}{t_p}\right)^2-\left(\frac{\rho^*}{t_p}\right)\right\}-r_s\cdot\left(\frac{\rho^*}{t_p}\right)^2\right\}\end{aligned} \tag{30}$$

and in case of symmetry:

$$\begin{aligned}\sigma_e &= \frac{1}{\rho^*}\int_0^{\rho^*} \sigma_n(r)\mathrm{d}r\\ &= \sigma_s\cdot\left(\frac{t_p}{\rho^*}\right)\cdot\left\{\left[1-2r_s\left\{1-f\left(\frac{r}{t_p}=\frac{1}{2}\right)\right\}\right]\cdot\right.\\ &\left(\left(\frac{\rho^*}{t_p}\right)^{\lambda_s}\mu_s(\lambda_s+1)[\cos\{(\lambda_s+1)\beta\}-\right.\\ &\chi_s\cos\{(\lambda_s-1)\beta\}]+\\ &\left(\frac{\rho^*}{t_p}\right)^{\lambda_a}\mu_a(\lambda_a+1)[\sin\{(\lambda_a+1)\beta\}-\\ &\chi_a\sin\{(\lambda_a-1)\beta\}]+\\ &\left.C_{bw}\cdot\left\{2\left(\frac{\rho^*}{t_p}\right)^2-\left(\frac{\rho^*}{t_p}\right)\right\}\right)+\\ &\left.r_s\cdot\left\{2\cdot f\left(\frac{r}{t_p}=\frac{1}{2}\right)-1\right\}\cdot\left[\left\{1-f\left(\frac{r}{t_p}=\frac{1}{2}\right)\right\}\cdot\left(\frac{\rho^*}{t_p}\right)-\left(\frac{\rho^*}{t_p}\right)^2\right]\right\}.\end{aligned} \tag{31}$$

In order to obtain a most likely micro- and meso-structural length estimate, ρ^* can be added to the parameter vector $\boldsymbol{\theta}$; $S = S_e = \Delta\sigma_e(\rho^*)$. Adopting the MCF-HCF fatigue resistance curve formulations (Section 2), the effective notch stress concept performance will be investigated for HS's type C, B and A. Since for MCF-HCF fatigue of welded joints the weld toe notches remain the governing failure locations (Section 2), a Weakest Link theory [20,117,118] based at/near-surface to sub-surface transition correction is not required.

Exponential mean stress models have been developed in order to improve the life time estimates in case of relatively low stress range and high mean stress, like for as-welded joints exposed to MCF-HCF. Walker's mean stress model [3,119] is an important one, incorporating the 2 components required to characterise a loading & response cycle in space, e.g. a response (stress) range $\Delta\sigma = (\sigma_{max} - \sigma_{min})$ and a response (stress) ratio $r_r = (\sigma_{min}/\sigma_{max})$:

$$S_{e,eff} = \Delta\sigma_{e,eff} = \frac{\Delta\sigma_e}{(1-r_r)^{1-\gamma}}. \tag{32}$$

The loading & response ratio coefficient γ is a fitting parameter and is added to the parameter vector $\boldsymbol{\theta}$ as well; $S = S_{e,eff} = \Delta\sigma_{e,eff}(\rho^*, \gamma)$.

Welded joint HS type {C, B, A} resistance data regression analysis results (Table 2) show that for all MCF-HCF models the fatigue life time N is most likely log(Normal) distributed, as reflected in the smaller AIC values. The flexibility of the log(Weibull) distribution to provide skewness is not required. The RFL models performance exceeds that of the BB model. Fatigue strength limit S_∞ seems to be most likely log (Weibull) distributed, meaning that fatigue induced failure turns from a 'normal' event into an 'extreme' (distributed) one, corresponding to an increased fatigue resistance data scatter when shifting from MCF to HCF (Section 2).

The parameter maximum likelihood estimates (MLE's) for the MCF region $\{\widehat{\log(C)}, \widehat{m}, \widehat{\gamma}, \widehat{\rho^*}\}$ are similar for all models (Table 3), since the formulations show only different HCF behaviour. As can be expected for

Table 2
HS type {C, B, A} MCF-HCF S_e-N regression analysis results.

Model	$f(\log(N), \mu, \sigma)$	$f(\log(S_\infty), \mu, \sigma)$	AIC
BB	Normal		3739
	Weibull		4123
ORFL	Normal	Normal	3114
	Normal	Weibull	1258
	Weibull	Normal	3150
	Weibull	Weibull	3129
BRFL	Normal	Normal	3077
	Normal	Weibull	1225
	Weibull	Normal	3474
	Weibull	Weibull	3472
GRFL	Normal	Normal	3054
	Normal	Weibull	1187
	Weibull	Normal	3136
	Weibull	Weibull	3104

Table 3
HS type {C, B, A} S_e-N $\{f_N(N), f_W(S_\infty)\}$ model parameter estimates.

Parameter	BB	ORFL	BRFL	GRFL
$\log(C)$	12.74	11.93	12.71	12.02
m	3.30	3.03	3.30	3.04
γ	0.90	0.91	0.92	0.92
ρ^*	0.93	1.13	1.11	1.14
σ_N	0.30	0.17	0.23	0.20
S_t	112			
m_t	4.38			
$S_{\infty,\mu}$		13	43	39
$S_{\infty,\sigma}$		2.9	2.0	2.1
ρ_{S_∞}				0.6

Table 4
HS type {C, B, A} S_e-N GRFL $\{f_N(N), f_W(S_\infty)\}$ model scaled co-variance matrix.

Parameter	$\log(C)$	m	γ	ρ^*	σ_N	$S_{\infty,\mu}$	$S_{\infty,\sigma}$	ρ_{S_∞}
$\log(C)$	1.00	0.97	0.04	−0.17	0.37	−0.31	0.44	−0.44
m		1.00	−0.04	−0.01	0.31	−0.36	0.46	0.36
γ			1.00	0.10	0.05	0.13	−0.06	−0.06
ρ^*				1.00	−0.06	−0.16	0.04	0.00
σ_N					1.00	0.18	−0.13	−0.62
$S_{\infty,\mu}$						1.00	−0.91	−0.41
$S_{\infty,\sigma}$							1.00	0.22
ρ_{S_∞}								1.00

log–log linear MCF behaviour, the scaled co-variance matrix (Table 4) shows a highly correlated intercept $\log(C)$ and slope m. The m estimates are comparable to the results obtained for MCF resistance data only [11] and close to the typical design value $m = 3$ [25–27]. The MCF $\{\log(C), m, \gamma, \rho^*, \sigma_N\}$ parameter confidence intervals ($c_l = 0.75$) in between the lower and upper bounds (CLB and CUB) are small (Table 5), since a significant amount of MCF resistance data is involved.

For all models, Walker's loading & response ratio coefficient MLE $\hat{\gamma}$ indicates that the stress range contributes ~ 90 [%] to the effective stress value (Table 3). The remaining ~ 10 [%] is coming from the mean stress, incorporating both the welding induced residual- and the mechanical loading & response component. The welding induced residual stress is typically highly tensile, explaining why the contribution of the mechanical part is limited [3,11], as reflected in the $\hat{\gamma}$ value itself as well as the limited $\log(C) - \gamma$ correlation (Table 4).

Embedded in the critical distance theory [120], micro- and meso-structural length or distance ρ^* is loading & response level dependent because of changing crack initiation and growth contributions. For welded joints in steel structures an average value of $\rho^* = 0.4$ [mm] is typical [9]. However, size effects have been observed, because the zone 1, 2 and 3 contributions are just partially included. A range of t_p dependent ρ^* values have been obtained [121] and the model estimates $\widehat{\rho^*} \sim 1$ [mm] are in between (Table 3). When shifting from MCF to HCF, ρ^* may decrease as shown up to some extent for the BB model 3 providing a most likely (average) MCF-HCF estimate, since the fatigue life time becomes initiation rather than growth dominated. For the RFL models, $S_\infty = S_{e,\infty}$ principally incorporates the HCF characteristic ρ^* behaviour implicitly, meaning ρ^* remains principally an average MCF estimate. The $\log(C) - \rho^*$ correlation (Table 4) confirms that ρ^* effectively contributes to the fatigue strength characterisation of welded joints.

Comparing the life time standard deviation MLE $\widehat{\sigma_N}$ for the different models, the BB value is quite large (Table 3) because of the combined MCF-HCF life time scatter. For the RFL models the MCF $\widehat{\sigma_N}$ is smaller as reflected in the AIC values (Table 2). Comparing the ORFL and GRFL model $\widehat{\sigma_N}$ to the BRFL model value, a gradual MCF-HCF transition is better than an abrupt one (Table 3). The MCF fatigue life time scatter is predominantly correlated to the MCF strength parameters $\log(C)$ and m (Table 4), as expected for log–log linear behaviour.

Analysing the HCF strength characteristics, the BB model transition strength S_t confidence is quite low: $92 \leqslant \widehat{S_t} \leqslant 138|_{cl=0.75}$. Note that $N_t(\widehat{S_t}) \sim 10^6$is already below the characteristic R97.7 FAT class value definition at $N = 2{\cdot}10^6$ cycles. Because of the large amount of data on the right side of N_t, the slope confidence is relatively high: $4.15 \leqslant \widehat{m_t} \leqslant 4.66|_{cl=0.75}$. The MLE $\widehat{m_t}$ is quite close to the Eurocode 3 design value $m_t = 5$ and far away from the IIW one: $m_t = 22$. In comparison to the RFL model $S_{\infty,\mu}$ values, the BB model MCF-HCF fatigue transition strength S_t is large as a result of a naturally increasing slope for decreasing fatigue strength: $m_t < \infty$. For the RFL models, the joined fatigue life time and fatigue limit scatter is explicitly incorporated. Although $\widehat{\sigma_N}$ is slightly larger for the GRFL model in comparison to the ORFL model, the fatigue limit strength scatter is significantly smaller, explaining the excellent GRFL model performance (Table 2). The GRFL model AIC values indicate that a (log)Weibull distributed S_∞ provides a better fit than a (log)Normal distributed one, suggesting $f_W(S_\infty)$ is right-skewed (Fig. 15). The welded joint fatigue strength limit implicitly includes the HCF notch effectivity and mean (residual) stress effects, meaning $S_{e,\infty}(\mu, \sigma)$ is a material characteristic parameter like $\rho*$ [122,123] and γ. The GRFL model MCF-HCF transition curvature parameter ρ_{S_∞} is close to 0, reflecting near BRFL behaviour (Fig. 16).

The fatigue limit strength distribution location and scale parameters $\{S_{\infty,\mu}, S_{\infty,\sigma}\}$ are naturally highly correlated (Table 4). As expected for a 2-slope fatigue resistance formulation like the GRFL model, the log–log linear MCF $\{\log(C), m, \sigma_N\}$- and the fatigue strength limit HCF $\{S_{\infty,\mu}, S_{\infty,\sigma}\}$ parameters show a high correlation as well. The joined fatigue life time and fatigue strength limit PDF and CDF involved in the RFL models are reflected in the $S_\infty(\mu, \sigma)$-σ_N correlations. Providing a dedicated MCF-HCF transition curvature, ρ_{S_∞} has a key parameter role in correlating the MCF $\{\log(C), m, \sigma_N\}$- and HCF $\{S_{\infty,\mu}, S_{\infty,\sigma}\}$ parameters, showing the added value of the GRFL model. The HCF $\{S_{\infty,\mu}, S_{\infty,\sigma}, \rho_{S_\infty}\}$ parameter confidence intervals are relatively small (Table 5), although for $S_{\infty,\mu}$ more HCF resistance data would increase the confidence even more.

Table 5
HS type {C, B, A} S_e-N GRFL $\{f_N(N), f_W(S_\infty)\}$ model parameter MLE's and CB's.

Parameter	C75LB	MLE	C75UB
$\log(C)$	11.90	12.02	12.13
m	2.99	3.04	3.08
γ	0.91	0.92	0.93
ρ^*	1.07	1.14	1.24
σ_N	0.19	0.20	0.20
$S_{\infty,\mu}$	35	39	43
$S_{\infty,\sigma}$	2.0	2.1	2.3
ρ_{S_∞}	0.5	0.6	0.7

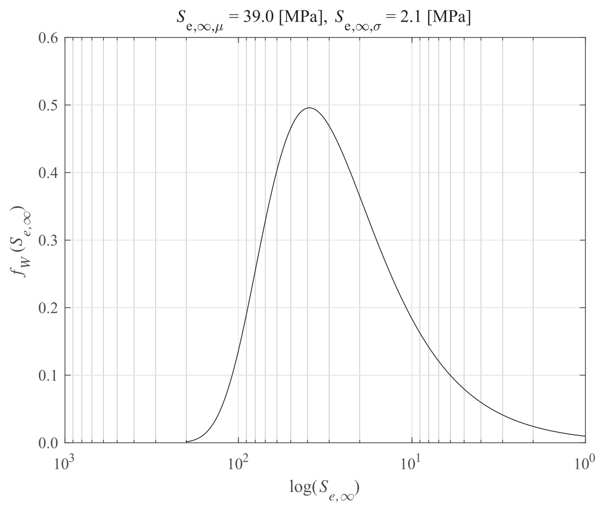

Fig. 15. GRFL model (log)Weibull $S_{e,\infty}(\mu, \sigma)$ distribution.

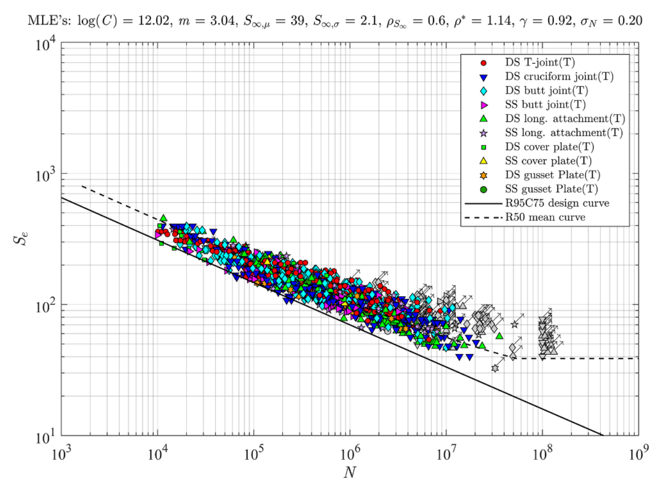

Fig. 16. GRFL $\{f_N(N), f_W(S_\infty)\}$ model based HS type {C, B, A} $S_e - N$ fatigue resistance data and design curve.

The GRFL model based $S_e - N$ data presentation for log(Normal) fatigue life time and log(Weibull) fatigue strength limit distributions shows an increasing fatigue resistance scatter when shifting from the MCF to the HCF region, justifying the joined $\{f(N), f(S_\infty)\}$ 2-slope formulation (Fig. 16). However, establishing a design curve, e.g. the R95C75 quantile, near 1-slope behaviour is observed for the fatigue life time range $N = 10^4 \ldots 10^9$, meaning for engineering purposes a LB model approximation rather than a piecewise continuous bi-linear MCF-HCF formulation according to guidelines, standards and classification notes [26,27,34] should be adopted.

Although generalised fatigue strength criteria formulations like the effective notch stress allow for combined HS type {C, B, A} analysis, separate HS type investigations could be used to reveal specific characteristics. However, a one-to-one comparison would be difficult, since the available amount of HS type C, B and A data as well as the variety in loading & response conditions and geometry is different.

Anyway, the separate HS type C, B and A MCF parameters are similar, as reflected in the merged fatigue resistance data cloud for the individual HS types (Fig. 17). The fatigue damage mechanism is similar because of a similar slope m. In terms of (correlated) intercept $\log(C)$, loading & response ratio coefficient γ and the micro- and meso-structural length parameter ρ^*, the effective fatigue strength is similar as well. Significant welding quality induced differences - including mSC size variations (Section 2) and residual stress - affecting the HS type C, B and A fatigue strength and life time are not observed. Investigating the fatigue strength consequences for a range of HS type B related artificial plate thickness values ($5 \leqslant t_p' \leqslant 30$), $t_p' = 20$ [mm] provides the best fit (Table 6).

The separate HC type C, B and A fatigue life time scatter MLE's $\widehat{\sigma_N} = \{0.20, 0.16, 0.16\}$ show a larger HS type C value, as a result of the large amount of data (T-joints, cruciform joints, butt joints; Table 1). The combined HS type {C, B, A} MLE $\widehat{\sigma_N} = 0.20$ shows that the HS type C scatter is in charge. At the same time, the HS type B and A data does not increase the combined HS type MLE. Similar HCF behaviour for the separate HS type C, B and A data has been observed as well, showing that the effective notch stress as generalised fatigue strength criterion extends from the MCF to the HCF region.

3.5. Total stress concept

Assuming that arc-welded joints inevitably contain flaws, defects at the weld toe notches, fatigue damage will primarily be a matter of notch affected micro- and far field dominated macro-crack growth, justifying a cracked geometry fatigue strength criterion involving the weld notch stress intensity distribution (Section 3.2). Cyclic loading & response conditions turn K_I into a crack growth driving force ΔK_I and defects may develop into cracks. The crack growth rate ($\mathrm{d}a/\mathrm{d}n$) of micro-cracks emanating at notches show elastoplastic wake field affected anomalies [3]. Modifying Paris' equation, a two-stage micro- and macro-crack growth relation similarity has been established to include both the weld notch- and far field characteristic contributions: $\left(\frac{\mathrm{d}a}{\mathrm{d}n}\right) = C \cdot Y_n^n \cdot (\Delta\sigma_{s,eff} \cdot Y_f \cdot \sqrt{\pi a})^m$. Notch elastoplasticity coefficient n is loading & response level dependent and turns non-monotonic crack growth behaviour in the MCF region into monotonically increasing crack growth behaviour in the HCF region. Walker's mean stress model has been used to incorporate the effective structural stress range $\Delta\sigma_{s,eff} = \Delta\sigma_s/(1 - \eta_{lr})^{1-\gamma}$. Crack growth model integration provides a (MCF) 1-slope resistance relation, correlating the fatigue life time N and total stress (cracked geometry) fatigue strength criterion S_T [3,6]:

$$S_T = \frac{\Delta\sigma_s}{(1 - \eta_{lr})^{1-\gamma} \cdot I_N^{\frac{1}{m}} \cdot t_p^{\frac{2-m}{2m}}} \tag{33}$$

with

$$I_N = \int_{\frac{a_i}{t_p}}^{\frac{a_f}{t_p}} \frac{1}{\left\{Y_n\left(\frac{a}{t_p}\right)\right\}^n \cdot \left\{Y_f\left(\frac{a}{t_p}\right)\right\}^m \cdot \left(\frac{a}{t_p}\right)^{\frac{m}{2}}} \mathrm{d}\left(\frac{a}{t_p}\right).$$

Scaling parameter $t_p^{2-m/2m}$ takes the response gradient induced size

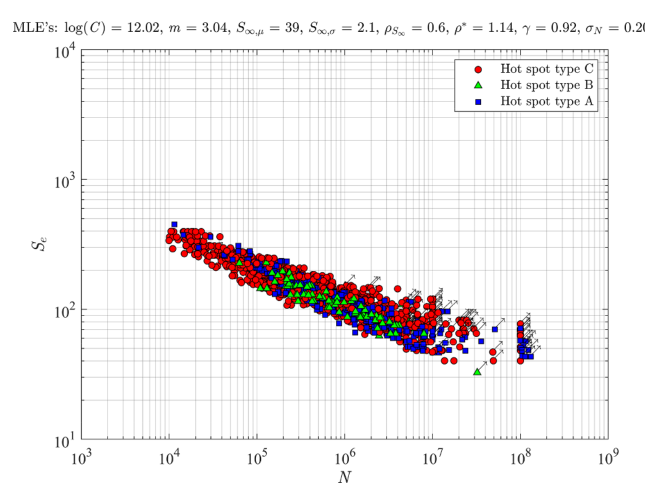

Fig. 17. GRFL $\{f_N(N), f_W(S_\infty)\}$ model based HS type C, B and A S_e-N fatigue resistance data.

Table 6
GRFL $\{f_N(N), f_W(S_\infty)\}$ model based most likely t_p'.

t_p' [mm]	5	10	20	30
AIC [–]	1270	1272	1187	1229

effects into account. For HS's type C and A, either $t_p = t_b$ or $t_p = t_c$. Plate thickness $t_p = t_p'$ for HS's type B. Notch crack growth integral I_N requires an initial crack size a_i. Adopting a constant (a_i/t_p) incorporates an average t_p induced weld volume effect.

In order to obtain a most likely (average) elastoplasticity coefficient and loading & response ratio coefficient estimate, n and γ can be added to the parameter vector θ (Section 2). Adopting the MCF-HCF fatigue resistance curve formulations (Section 2), the total stress concept performance will be investigated for HS's type {C, B, A}. An at/near-surface to sub-surface fatigue damage location transition like for plane geometries when shifting from MCF tot HCF is not involved, meaning any fish-eye induced micro-crack growth behaviour does not have to be incorporated [21,124–126].

Welded joint HS type {C, B, A} S_T-N resistance data regression analysis results (Table 7) show that the BRFL $\{f_N(N), f_W(S_\infty)\}$ model provides the best performance. However, the GRFL $\{f_N(N), f_W(S_\infty)\}$ model will be adopted because of similar performance, allowing for a one-to-one comparison of the effective notch stress- and total stress concept results as well. Comparing the S_e (Table 2) and S_T (Table 7) based AIC values, a slightly better effective notch stress concept performance is suggested.

Investigating the AIC for a range of (a_i/t_p) values (Fig. 18), an average MLE has been obtained first: $\widehat{(a_i/t_p)} = 0.006$. For the considered fatigue resistance data (Table 1), t_p is ranging from 2 to 160 [mm], meaning a_i should be in between 0.012 and 0.96 [mm]. For the plate thickness mode value $t_p \sim 15$ [mm], mode $a_i \sim 0.09$ [mm]. Although $\widehat{(a_i/t_p)}$ implicitly may include more than the real welding induced defect size since a back calculation technique is adopted, the a_i mode is close to a real defect size estimate: $a_i < 0.05$ [127–129].

All models provide similar MCF MLE's $\{\widehat{\log(C)}, \widehat{m}, \widehat{\gamma}, \widehat{n}\}$ (Table 8) and the confidence intervals are small, as shown for the GRFL model (Table 10). Adopting either an intact or cracked fatigue strength criterion, i.e. S_e or S_T, does not affect slope m. The majority of the welded joint fatigue life time is spent in the notch affected region, as explicitly incorporated using ρ^* and Y_n^n for respectively S_e and S_T, meaning both criteria incorporate the same physics. Because of the large $\log(C) - m$ correlation (Table 9), intercept $\log(C)$ is similar for S_e and S_T as well.

Walker's loading & response ratio coefficient MLE $\widehat{\gamma}$ shows that S_T is predominantly stress range determined (Table 8). Correlation to the $\{\log(C), m\}$ MCF parameters (Table 9) is more significant than for S_e (Table 4), most likely since for S_T the range and mean stress (intensity) contribution over t_p is considered, whereas S_e incorporates only a partial contribution over ρ^*.

For the same reason, n affects the log–log linear MCF behaviour much more than ρ^* does (Table 4 and 9). Elastoplasticity coefficient $\widehat{n} \sim 3...4$ and reflects non-monotonic crack growth behaviour [3], as expected in the MCF region. Like ρ^*, n is an average value since for decreasing response level the amount of notch and crack tip induced plasticity decreases. The relatively high n value includes a cyclic and mean (welding induced residual) response contribution. When shifting from MCF to HCF, n decreases since the notch and crack tip affected response becomes predominantly elastic, introducing monotonically increasing crack growth behaviour. However, principally $S_\infty = S_{T,\infty}$ incorporates the HCF characteristic n behaviour implicitly, meaning n remains an MCF estimate.

Because of the combined MCF-HCF life time scatter, the BB MLE $\widehat{\sigma_N}$ is quite large (Table 8). For the RFL models the MCF $\widehat{\sigma_N}$ is smaller as reflected in the AIC values (Table 7) and similar to σ_N as obtained for S_e as fatigue strength criterion. Still, a gradual MCF-HCF transition is better than an abrupt one (Table 8). The MCF $\widehat{\sigma_N}$ is highly correlated to the MCF parameters $\log(C)$, m, even n, as well as the HCF parameter $S_\infty(\mu, \sigma)$. Whereas ρ^* does not change the stress distribution characteristics, n turns MCF related non-monotonic crack growth into HCF related monotonically increasing crack growth behaviour.

The GRFL model balances the joined MCF-HCF fatigue life time and fatigue strength limit scatter $\{f_N(N), f_W(S_\infty)\}$ (Table 7). The slightly better performance of the BRFL model (Table 8) is reflected in the small GRFL model MCF-HCF transition curvature parameter ρ_{S_∞} (Fig. 19). The $S_{\infty,\sigma}$ scatter for S_T is relatively large in comparison to the results for S_e. Comparing the $\{S_{\infty,\mu}, S_{\infty,\sigma}\}$ confidence interval for the S_e and S_T fatigue strength criteria (Table 5 and 10), the S_T results are worse.

The GRFL $\{f_N(N), f_W(S_\infty)\}$ model provides (almost) the best fit. Like for the effective notch stress concept, the R95C75 quantile (Fig. 19) reflecting a probability level of survival $p_s = 0.95$ and a confidence level $c_l = 0.75$, a MCF-HCF design curve, shows near 1-slope behaviour for the fatigue life time range $N = 10^4...10^9$.

The merged fatigue resistance data cloud for the individual HS types (Fig. 20) suggests similar S_T based fatigue resistance behaviour. Comparing the separate HC type C, B and A fatigue life time scatter MLE's $\widehat{\sigma_N} = \{0.19, 0.15, 0.16\}$ to the combined HS type {C, B, A} MLE $\widehat{\sigma_N} = 0.21$ shows that the HS type C scatter is in charge.

The data scatter increases when shifting from the crack growth dominated MCF- to the crack initiation governing HCF region (Fig. 19). Adopting a fatigue strength criterion naturally corresponding to the HCF region showing the largest data scatter - like S_e as crack initiation related intact geometry parameter rather than S_T as crack growth related cracked geometry parameter - makes sense and may explain the better effective notch stress concept performance. At the same time, changing the notch crack growth behaviour from non-monotonic to monotonically increasing for S_T using n might be more drastic than changing the notch stress effectivity for S_e using ρ^*, in order to obtain dedicated MCF and HCF characteristic behaviour. In order to improve the total stress concept performance, a loading & response level dependent elastoplasticity coefficient n could be introduced. Alternative to a one parameter MCF-HCF modelling approach, a two parameter approach could be adopted, modelling respectively crack growth governing MCF using S_T and crack initiation dominated HCF using S_e. However, a natural rather than a predefined transition is a challenge [2].

4. Conclusions

For steel renewable energy marine structures like floating offshore wind turbines, the arc-welded joints are typically the governing fatigue

Table 7
HS type {C, B, A} MCF-HCF $S_T - N$ regression analysis results.

Model	$f(\log(N), \mu, \sigma)$	$f(\log(S_\infty), \mu, \sigma)$	AIC
BB	Normal		3744
	Weibull		4296
ORFL	Normal	Normal	3211
	Normal	Weibull	1337
	Weibull	Normal	3330
	Weibull	Weibull	3277
BRFL	Normal	Normal	3106
	Normal	Weibull	1255
	Weibull	Normal	3486
	Weibull	Weibull	3136
GRFL	Normal	Normal	3126
	Normal	Weibull	1267
	Weibull	Normal	3310
	Weibull	Weibull	3255

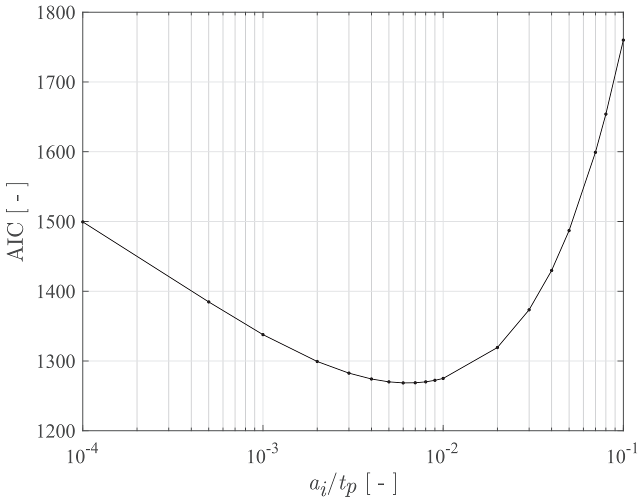

Fig. 18. GRFL $\{f_N(N), f_W(S_\infty)\}$ model based HS type {C, B, A} S_T most likely average initial crack size estimate.

Table 8
HS type {C, B, A} S_T-N $\{f_N(N), f_W(S_\infty)\}$ model parameter estimates.

Parameter	BB	ORFL	BRFL	GRFL
$\log(C)$	14.27	13.08	13.56	13.12
m	3.60	3.20	3.35	3.22
γ	0.87	0.90	0.90	0.91
n	4.01	3.52	3.64	3.36
σ_N	0.30	0.19	0.23	0.21
S_t	100			
m_t	5.3			
$S_{\infty,\mu}$		9	68	47
$S_{\infty,\sigma}$		5.3	2.1	2.7
ρ_{S_∞}				0.4

Table 9
HS type {C, B, A} S_T-N GRFL $\{f_N(N), f_W(S_\infty)\}$ model scaled co-variance matrix.

Parameter	$\log(C)$	m	γ	n	σ_N	$S_{\infty,\mu}$	$S_{\infty,\sigma}$	ρ_{S_∞}
$\log(C)$	1.00	0.96	−0.17	0.64	0.48	0.14	−0.05	−0.54
m		1.00	−0.14	0.44	0.40	0.07	0.00	−0.44
γ			1.00	−0.17	−0.05	−0.05	0.02	0.06
n				1.00	0.29	0.22	−0.09	−0.31
σ_N					1.00	0.43	−0.41	−0.73
$S_{\infty,\mu}$						1.00	−0.95	−0.63
$S_{\infty,\sigma}$							1.00	0.55
ρ_{S_∞}								1.00

sensitive locations. The characteristic welded joint far field response spectrum is predominantly linear elastic, meaning the fatigue resistance is MCF-HCF defined. Adopting different MCF-HCF fatigue resistance curve formulations, the effective notch stress concept and total stress concept performance have been investigated for arc-welded joint HS's type {C, B, A}, involving respectively a HCF crack initiation related intact geometry fatigue strength criterion (S_e) and a MCF crack growth related cracked geometry one (S_T).

Although fatigue strength limit behaviour will remain a hypothesis anyway and the S_∞ induced cyclic plasticity requirement might be identically satisfied, a RFL model explicitly incorporating the MCF life time and HCF strength limit scatter shows from statistical point of view the best performance.

The most likely PDF and CDF turned out to be the (log)Normal and (log)Weibull ones for respectively the fatigue life time and fatigue strength limit. The (log)Weibull distributed fatigue limit reflects the increasing scatter when shifting from the MCF to the HCF region, meaning fatigue induced failure becomes an extreme event. The (log) Normal distributed fatigue life time reflects the random mSC and MSC nature.

Taking advantage of accurate weld notch stress distribution (intensity) formulations, for both the predominantly MCF related S_T and principally HCF related S_e the GRFL model provides the most accurate fatigue strength and life time estimates.

Similar MCF performance is obtained for S_e and S_T. Although crack growth dominates the MCF damage process, the results for an initiation related criterion like S_e and a natural crack growth related criterion like S_T are similar. The S_e average MCF material characteristic micro- and

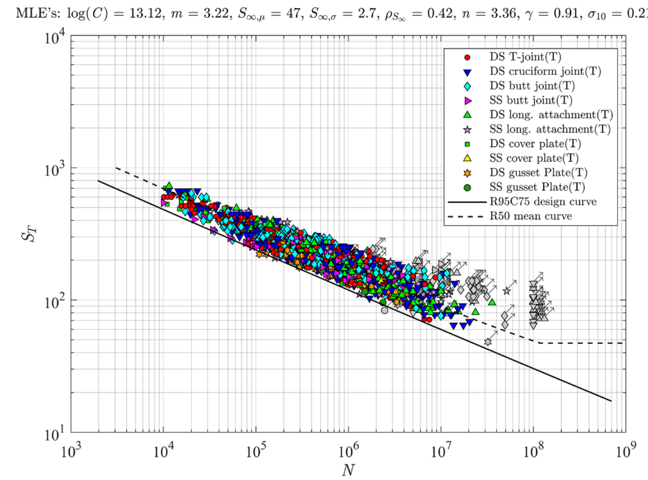

Fig. 19. GRFL $\{f_N(N), f_W(S_\infty)\}$ model based HS type {C, B, A} $S_T - N$ fatigue resistance data and design curve.

Table 10
HS type {C, B, A} S_T-N GRFL $\{f_N(N), f_W(S_\infty)\}$ model parameter MLE's and CB's.

Parameter	C75LB	MLE	C75UB
$\log(C)$	13.00	13.12	13.50
m	3.18	3.22	3.26
γ	0.89	0.91	0.92
n	3.18	3.36	3.57
σ_N	0.20	0.21	0.22
$S_{\infty,\mu}$	40	47	68
$S_{\infty,\sigma}$	2.4	2.7	3.1
ρ_{S_∞}	0.3	0.4	0.5

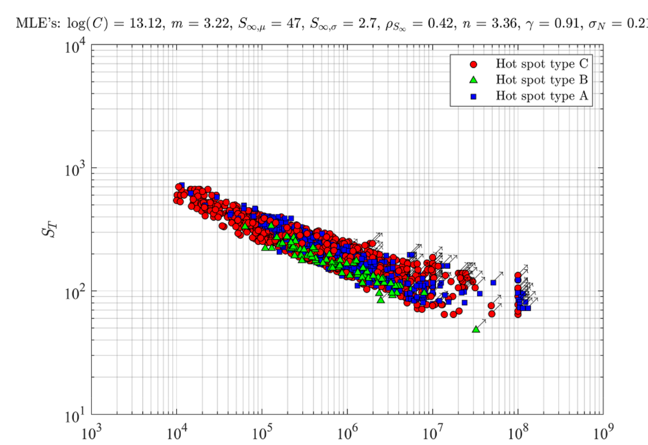

Fig. 20. GRFL $\{f_N(N), f_W(S_\infty)\}$ model based HS type C, B and A S_T-N fatigue resistance data.

submeso-structural length $\widehat{\rho^*} \sim 1$[mm] exceeds the typical value of 0.4, but is still in the range of observed values in literature. The S_T MCF characteristic elastoplasticity coefficient $\hat{n} \sim 3$ reflects notch and residual stress induced non-monotonic crack growth. HCF ρ^* and n contributions are implicitly included in $S_\infty(\mu, \sigma)$.

Comparing the S_e and S_T HCF performance, the S_e results are better as particularly reflected in the $S_\infty(\mu, \sigma)$ confidence bounds. Adopting S_e rather than S_T as fatigue strength criterion naturally corresponding to the HCF region showing the largest data scatter makes sense and may explain the overall effective notch stress concept performance. At the same time, changing the S_T related notch crack growth behaviour using n from non-monotonic to monotonically increasing in order to obtain dedicated MCF and HCF characteristic behaviour might be more drastic than changing the notch stress effectivity for S_e using ρ^* since the $\sigma_n(r/t_p)$ behaviour itself does not change.

Since the HCF resistance scatter is relatively large, the MCF-HCF GRFL model design curves show approximately 1-slope behaviour, meaning that for design purposes a LB model approximation rather than a piecewise continuous bi-linear MCF-HCF formulation according to guidelines, standards and classification notes [34,26,27] should be adopted.

Declaration of Competing Interest

The authors declare to have no known competing financial interests or personal relationships that could have appeared to influence the work reported in this paper.

Acknowledgment

The financial support from the China Scholarship Council (Grant No. 201606950015) is gratefully acknowledged.

References

[1] Schijve J. Fatigue of structures and materials. Springer; 2009. iSBN: 978-402068089.
[2] Den Besten JH. Fatigue damage criteria classification, modelling developments and trends for welded joints in marine structures. Ships Offshore Struct 2018;13(8):787–808. https://doi.org/10.1080/17445302.2018.1463609.
[3] Den Besten JH, Fatigue resistance of welded joints in aluminium high-speed craft: a total stress concept, Ph.D. thesis, Delft University of Technology; 2015.
[4] Stehly T, Beiter P, Heimiller D, Cost of wind energy review, Tech. rep., National Renewable Energy Laboratory; 2017.
[5] Beiter P, Musial W, Smith A, Kilcher L, Damiani R, Maness M, Sirnivas S, Stehly T, Gevorgian V, Mooney M, Scott G, A spatial-economic cost reduction pathway analysis for u.s. offshore wind energy development from 2015-2030, Tech. rep., National Renewable Energy Laboratory; 2016.
[6] International Renewable Energy Agency, Floating foundations: a game changer for offshore wind power, Tech. rep., International Renwable Energy Agency; 2016.
[7] Neuber H, Kerbspannungslehre, Springer-Verlag; 1937, iSBN: 3-540-67657-0.
[8] Zhang G, Sonsino CM, Sundermeier R. Method of effective stress for fatigue: Part ii–applications to v-notches and seam welds. Int J Fatigue 2012;37:24–40.
[9] Sonsino CM, Fricke W, de Bruyne F, Hoppe A, Ahmada A, Zhang G. Notch stress concepts for the fatigue assessment of welded joints – background and applications. Int J Fatigue 2012;34:2–16.
[10] Radaj D, Lazzarin P, Berto F. Generalised neuber concept of fictitious notch rounding. Int J Fatigue 2013;51:105–15.
[11] Qin Y, den Besten H, Palkar S, Kaminski ML. Fatigue design of welded double-sided t-joints and double-sided cruciform joints in steel marine structures: a total stress concept. Fatigue Fract Eng Mater Struct 2019;42(12):2674–93.
[12] Carpinteri A, Boaretto J, Fortese G, Giordani F, Iturrioz I, Ronchei C, Scorza D, Vantadori S. Fatigue life estimation of fillet-welded tubular t-joints subjected to multiaxial loading. Int J Fatigue 2017;101:263–70.
[13] Vantadori S, Iturrioz I, Carpinteri A, Greco F, Ronchei C. A novel procedure for damage evaluatıon of fıllet-welded joınts. Int J Fatigue 2020;136:105599.
[14] Pyttel B, Schwerdt D, Brunner I, B C. Fatigue strength and failure mechanisms in the VHCF-region. Anales de Mecanica de la Fractura 2011;28:2–8.
[15] Bathias C, Drouillac L, Le Francois P. How and why the fatigue s-n curve doesnot approach a horizontal asymptote. Int J Fatigue 2001;23:S143–51.
[16] Bathias C. There is no infinite fatigue life in metallic materials. Fatigue Fract Eng Mater Struct 1999;22:559–65.
[17] Berger C, Pyttel B, Trossman T. Very high cycle fatigue tests with smooth and notched specimens and screws made of light metal alloys. Int J Fatigue 2006;28:1640–6.
[18] Dekking FM, Kraaikamp C, Lopuhaä HP, Meester LE, A Modern Introduction to Probability and Statistics: Understanding why and how, Springer-Verlag London; 2005, iSBN: 978-1-85233-896-1.
[19] Mughrabi H. Specific features and mechanisms of fatigue in the ultrahigh-cycle regime. Int J Fatigue 2006;28:1501–8.
[20] Pyttel B, Schwerdt D. C B, Very high cycle fatigue – is there a fatigue limit? Int J Fatigue 2011;33:49–58.
[21] Akiniwa Y, Miyamoto N, Tsuru H. K T, Notch effect on fatigue strength reduction of bearing steel in the very high cycle regime. Int J Fatigue 2006;28:1555–65.
[22] Schaumann P, Steppeler S. Fatigue tests of axially loaded butt welds up to very high cycles. Procedia Eng 2013;66:88–97.
[23] Cremer M, Zimmermann M, Christ HJ, Fatigue behaviour of welded aluminium alloy joints at very high cycles. In: 18th European conference on fracture: fracture of materials and structures from micro to macro scale; 2010.
[24] Cremer M, Zimmermann M, Christ HJ. High-frequency cyclic testing of welded aluminium alloy joints in the region of very high cycle fatigue (VHCF). Int J Fatigue 2013;57:120–30.
[25] Hobbacher AF. Recommendations for fatigue design of welded joints and components, Springer International; 2016, iSBN: 978-3319237565.
[26] CEN. Eurocode 3: Design of Steel Structures, Part 1-9 Fatigue, European Committee for Standardization; 2005.
[27] DNV-GL. Classification Notes No. 30.7 Fatigue Assessment of Ship Structures, DNV-GL; 2014.
[28] Pascual F, Meeker W. Estimating fatigue curves with the random fatigue-limit model. Technometrics 1999;41:277–89.
[29] D'Angelo L, Nussbaumer A. Estimation of fatigue s-n curves of welded joints using advanced probabilistic approach. Int J Fatigue 2017;97:98–113.
[30] Leonetty D, Maljaars J, Snijder H. Fitting fatigue test data with a novel s-n curve using frequentist and bayesian inference. Int J Fatigue 2017;105:128–43.
[31] Sonsino C. Course of sn-curves especially in the high-cycle fatigue regime with regard to component design and safety. Int J Fatigue 2007;29:2246–58.
[32] Sarkani S, Mazzuchi T, Lewandowski D, Kihl D. Runout analysis in fatigue investigation. Eng Fract Mech 2007;74:2971–80.
[33] Akaike H. Information theory and an extension of the maximum likelihood principle. In: 2nd int. symposium on information theory, Budapest; 1973. p. 267–81.
[34] Hobbacher AF, et al. Recommendations for fatigue design of welded joints and components. Springer; 2009.
[35] Ronold K, Lotsberg I. On the estimation of charateristic s-n curves with confidence. Mar Struct 2012;27:29–44.
[36] Lotsberg I. Fatigue design of marine structures. Cambridge University Press; 2016, iSBN: 978-1-107-12133.
[37] Fricke W. Recommended hot-spot analysis procedure for structural details of ships and FPSO's based on round-robin fe analyses. Int J Offshore Polar Eng 2002;12:40–7.
[38] Niemi E, Fricke W, Maddox S. Structural hot-spot stress approach to fatigue analysis of welded components - designer's guide. Springer; 2016, iSBN: 978–981-10-4458-3.
[39] Dong P. A structural stress definition and numerical implementation for fatigue analysis of welded joints. Int J Fatigue 2001;23(10):865–76.
[40] Dong P. A robust structural stress method for fatigue analysis of ship structures, in. Proceedings of the 22nd international conference on offshore mechanics and arctic engineering, OMAE 2003, ASME. 2003. p. 199–211.
[41] Radaj D, Sonsino C, Fricke W. Recent developments in local concepts of fatigue assessment of welded joints. Int J Fatigue 2009;31:2–11.
[42] Radaj D. State-of-the-art review on extended stress intensity factor concepts. Fatigue Fract Eng Mater Struct 2014;37:1–28.
[43] Radaj D. State-of-the-art review on the local strain energy density concept and its relation to the j-integral and peak stress method. Fatigue Fract Eng Mater Struct 2015;38:2–28.
[44] Fricke W. Recent developments and future challenges in fatigue strength assessment of welded joints. J Mech Eng Sci 2015;229:1224–39.
[45] Lazzarin P, Tovo R. A unified approach to the evaluation of linear elastic stress fields in the neighborhood of cracks and notches. Int J Fract 1996;78:3–19.
[46] Atzori B, Lazzarin P, Tovo R. Stress distributions for v-shaped notches under tensile and bending loads. Fatigue Fract Eng Mater Struct 1997;20(8):1083–92.
[47] Pook L. A 50-year retrospective review of three-dimensional effects at cracks and sharp notches. Fatigue Fract Eng Mater Struct 2013;36:699–723.
[48] Tada H, Paris PC, Irwin GR. The stress analysis of cracks handbook. ASME Press; 2000.
[49] Miki C, Mori T, Sakamoto K, Kashiwagi H. Size effect on the fatigue strength of transverse fillet welded joints. J Struct Eng 1987;33:393–402.
[50] SR202. Fatigue Design and Quality Control for Offshore Structures, Committee of Shipbuilding Research Association of Japan; 1991, in Japanese.
[51] Galtier A, Statnikov E, Irsid A. The influence of ultrasonic impact treatment on fatigue behaviour of welded joints in high-strength steel. Weld World 2004;48(5–6):61–6.
[52] Pedersen MM, Mouritsen OØ, Hansen MR, Andersen JG, Wenderby J. Comparison of post-weld treatment of high-strength steel welded joints in medium cycle fatigue. Weld World 2010;54(7–8):R208–17.
[53] Ahola A, Nykänen T, Björk T. Effect of loading type on the fatigue strength of asymmetric and symmetric transverse non-load carrying attachments. Fatigue Fract Eng Mater Struct 2017;40(5):670–82.
[54] Mecozzi E, Lecca M, Sorrentino S, Large M, Davies C, Gouveia H, Maia C, Erdelen-Peppler M, Karamanos S, Perdikaris P, Fatigue behaviour of high-strength steel-welded joints in offshore and marine systems (FATHOMS), Mecozzi, M. Lecca, S. Sorrentino-Office for Official Publ. of the European Communities; 2010. p. 179.

[55] Budano S, Kuppers M, Kaufmann H, Meizso A, Davies C. Application of high-strength steel plates to welded deck components for ships and bridges subjected to medium/high service loads. EUR 2007;22571.
[56] Statnikov E, Muktepavel V, Blomqvist A. Comparison of ultrasonic impact treatment (UIT) and other fatigue life improvement methods. Weld World 2002;46(3–4):20–32.
[57] Haagensen P, IIW's round robin and design recommendations for improvement methods. In: IIW conference on performance of dynamically loaded welded structures, San Francisco, vol. 305; 1997.
[58] Noordhoek C, Scholte H, Jonkers P, Koning C, Dijkstra O, Fatigue and fracture behavior of welded joints in high strength steel(Fe E 460), EUR(Luxembourg); 1993.
[59] Stoschka M, Di Leitner M, Fössl T, Posch G. Effect of high-strength filler metals on fatigue. Weld World 2012;56(3–4):20–9.
[60] Leitner M, Stoschka M, Eichlseder W. Fatigue enhancement of thin-walled, high-strength steel joints by high-frequency mechanical impact treatment. Weld World 2014;58(1):29–39.
[61] Kihl DP, Sarkani S. Thickness effects on the fatigue strength of welded steel cruciforms. Int J Fatigue 1997;19(93):311–6.
[62] Nykänen T, Marquis G, Björk T. Effect of weld geometry on the fatigue strength of fillet welded cruciform joints. In: Proceedings of the international symposium on integrated design and manufacturing of welded structures, Lappeenranta University of Technology, Lappeenranta; 2007.
[63] NIMS. Data sheets on Fatigue Strength of Non-Load-Carrying Cruciform Welded Joints of SM490B Steel for Welded Structures-Effect of Plate Thickness (Patr 1, Thickness 9 mm), NIMS Fatigue Datasheet No.96, National Research Institute for Metals; 2004. arXiv:http://smds.nims.go.jp/MSDS/pdf/sheet/F96J.pdf.
[64] Kuhlmann U, Bergmann J, Dürr A, Thumser R, Günther HP, Gerth U. Erhöhung der ermüdungsfestigkeit von geschweißten höherfesten baustählen durch anwendung von nachbehandlungsverfahren. Stahlbau 2005;74(5):358–65.
[65] Lindqvist J. fatigue strengths thickness dependence in welded construction, Ph.D. thesis, M. Sc. Thesis, Borlänge University, Sweden; 2002.
[66] Maddox SJ. The effect of plate thickness on the fatigue strength of fillet welded joints. The Welding Institute, Abington Hall, Abington, Cambridge CB 1 6 AL, UK, 1987. 48; 1987.
[67] NIMS. Data sheets on Fatigue Strength of Non-Load-Carrying Cruciform Welded Joints of SM570Q Steel for Welded Structures, NIMS Fatigue Datasheet No. 90, National Research Institute for Metals; 2002. arXiv:http://smds.nims.go.jp/MSDS/pdf/sheet/F90J.pdf.
[68] NIMS. Data sheets on Fatigue Strength of Non-Load-Carrying Cruciform Welded Joints of SM490B Steel for Welded Structures-Effect of Residual Stress, NIMS Fatigue Datasheet No.91, National Research Institute for Metals; 2003. arXiv:http://smds.nims.go.jp/MSDS/pdf/sheet/F91J.pdf.
[69] Kudryavtsev Y, Kleiman J, Lugovskoy A, Lobanov L, Knysh V, Voitenko O, Prokopenko G. Rehabilitation and repair of welded elements and structures by ultrasonic peening. Weld World 2007;51(7–8):47–53.
[70] NIMS. Data sheets on Fatigue Strength of Non-Load-Carrying Cruciform Welded Joints of SM490B Steel for Welded Structures-Effect of Plate Thickness (Patr 4, Thickness 40 mm), NIMS Fatigue Datasheet No.114, National Research Institute for Metals; 2011. arXiv:http://smds.nims.go.jp/MSDS/pdf/sheet/F114J.pdf.
[71] NIMS. Data sheets on Fatigue Strength of Non-Load-Carrying Cruciform Welded Joints of SM490B Steel for Welded Structures-Effect of Plate Thickness (Patr 3, Thickness 80 mm), NIMS Fatigue Datasheet No.108, National Research Institute for Metals; 2009. arXiv:http://smds.nims.go.jp/MSDS/pdf/sheet/F108J.pdf.
[72] NIMS. Data sheets on Fatigue Strength of Non-Load-Carrying Cruciform Welded Joints of SM490B Steel for Welded Structures-Effect of Plate Thickness (Patr 2, Thickness 160 mm), NIMS Fatigue Datasheet No.99, National Research Institute for Metals; 2006. arXiv:http://smds.nims.go.jp/MSDS/pdf/sheet/F99J.pdf.
[73] Ahiale GK, Oh YJ. Microstructure and fatigue performance of butt-welded joints in advanced high-strength steels. Mater Sci Eng: A 2014;597:342–8.
[74] Kang S. Thickness effect of fatigue on butt weld joints. In: TSCF 2016 shipbuilders meeting; 2016.
[75] Kim KN, Lee SH, Jung KS. Evaluation of factors affecting the fatigue behavior of butt-welded joints using sm520c-tmc steel. Int J Steel Struct 2009;9(3):185–93.
[76] Crupi V, Guglielmino E, Maestro M, Marinò A. Fatigue analysis of butt welded ah36 steel joints: thermographic method and design s–n curve. Mar Struct 2009;22(3):373–86.
[77] Costa J, Ferreira J, Abreu L. Fatigue behaviour of butt welded joints in a high strength steel. Procedia Eng 2010;2(1):697–705.
[78] Lixing H, Dongpo W, Wenxian W, Yufeng Z. Ultrasonic peening and low transformation temperature electrodes used for improving the fatigue strength of welded joints. Weld World 2004;48(3–4):34–9.
[79] Huther I, Lam A, Velluet L, Royer Y, Lieurade H. Methodology to define sn curves in connection with weld quality. Weld World 2005;49(9–10):102–10.
[80] NIMS. Data sheets on fatigue properties for butt welded joints on SM50B high tensile structural steel plate; 1978. arXiv:http://smds.nims.go.jp/MSDS/pdf/sheet/F5J.pdf.
[81] Weich I, Ummenhofer T, Nitschke-Pagel T, Dilger K, Chalandar HE. Fatigue behaviour of welded high-strength steels after high frequency mechanical post-weld treatments. Weld World 2009;53(11–12):R322–32.
[82] NIMS. Data sheets on fatigue properties for butt welded joints on SB42 carbon steel plate for boilers and other pressure vessels - effect of stress ratio, NIMS Fatigue Datasheet No.34, National Research Institute for Metals; 1983. http://smds.nims.go.jp/MSDS/pdf/sheet/F34J.pdf.
[83] Nakamura H, Nishijima S, Ohta A, Maeda Y, Uchino K, Kohno T, Toyomasu K, Soya I. A method for obtaining conservative sn data for welded structures. J Test Eval 1988;16(3):280–5.
[84] Radziminski JB, Lawrence FV, Wells TW, Mah R, Munse WH, Low cycle fatigue of butt weldments of HY-100 (t) and HY-130 (t) steel, Tech. Rep. 361, University of Illinois Engineering Experiment Station. College of Engineering. University of Illinois at Urbana-Champaign; 1970.
[85] Yagi J, Machida S, Tomita Y, Matoba M, Kawasaki T. Definition of hot spot stress in welded plate type structure for fatigue assessment (1st report). J Soc Naval Archit Jpn 1991;1991(169):311–8.
[86] Berg J, Stranghöner N. Fatigue behaviour of high frequency hammer peened ultra high strength steels. Int J Fatigue 2016;82:35–48.
[87] Lotsberg I. Assessment of fatigue capacity in the new bulk carrier and tanker rules. Marine Structures 2006;19:83–96.
[88] Jang C, Han J, Kang J, Kim Y, Jeon Y, Song H. Fatigue life assessment of welded joints considering crack propagation based on hot spot stress. In: OMAE congress; 2001.
[89] Gurney T, Trepka LN. Influence of local heating on fatigue behaviour of welded specimens. Br Weld J 1959;6:491–7.
[90] Pereira Baptista CA. Multiaxial and variable amplitude fatigue in steel bridges, Tech. rep., EPFL; 2016.
[91] Choi DH, Choi H, Lee D. Fatigue life prediction of in-plane gusset welded joints using strain energy density factor approach. Theoret Appl Fract Mech 2006;45(2):108–16.
[92] Yamada K, Sakai Y, Kikuchi Y, Fatigue of tensile plate with gussets and stop holes as crack arrest. In: Proceedings of the japan society of civil engineers, vol. 1984, Japan Society of Civil Engineers; 1984. p. 129–36.
[93] Gurney T. Further fatigue tests on mild steel specimens with artificially induced residual stresses. Br Weld J 1962;9.
[94] Lihavainen VM, Marquis G, Statnikov E. Fatigue strength of a longitudinal attachment improved by ultrasonic impact treatment. Weld World 2004;48(5–6):67–73.
[95] Matsumoto R, Ishikawa T, Takemura M, Hiratsuka Y, Kawano H. Extending fatigue life of out-of-plane gusset joint by bonding cfrp plates under bending moment. Int J Steel Struct 2016;16(4):1319–27.
[96] Maddox S. Influence of tensile residual stresses on the fatigue behavior of welded joints in steel. In: Residual stress effects in fatigue. ASTM International; 1982.
[97] Huo L, Wang D, Zhang Y. Investigation of the fatigue behaviour of the welded joints treated by tig dressing and ultrasonic peening under variable-amplitude load. Int J Fatigue 2005;27(1):95–101.
[98] Kainuma S, To K, Uchida D, Yagi N, Kubo H. Fatigue behaviour of out-of-plane gusset joints with one-side fillet weld. Weld Int 2015;29(12):913–21.
[99] Yamada K, Makino T, Baba C, Kikuchi Y. Fatigue analysis based on crack growth from toe of gusset end weld. In: Proceedings of the Japan Society of Civil Engineers, vol. 1980, Japan Society of Civil Engineers; 1980. p. 31–41.
[100] Marquis G. Long life spectrum fatigue of carbon and stainless steel welds. Fatigue Fract Eng Mater Struct 1996;19(6):739–53.
[101] Maddox S, Hopkin G, Holy A, Moura Branco C, Infante V, Baptista R, Schuberth S, Sonsino C, Küppers M, Marquis G, et al., Improving the fatigue performance of welded stainless steels, EUR (22809); 2007. p. 1–190.
[102] Kang S, Kim W. A proposed sn curve for welded ship structures. Weld J-New York 2003; 82 (7): 161–S.
[103] Kim IT. Fatigue strength improvement of longitudinal fillet welded out-of-plane gusset joints using air blast cleaning treatment. Int J Fatigue 2013;48:289–99.
[104] Kim IT, Kim HS, Dao DK, Ahn JH, Jeong YS. Fatigue resistance improvement of welded joints by bristle roll-brush grinding. Int J Steel Struct 2018;18(5):1631–8.
[105] Mori T, Shimanuki H, Tanaka M. Influence of steel static strength on fatigue strength of web-gusset welded joints with uit. J JSCE 2015;3(1):115–27.
[106] Togasaki Y, Tsuji H, Honda T, Sasaki T, Yamaguchi A. Effect of uit on fatigue life in web-gusset welded joints. J Solid Mech Mater Eng 2010;4(3):391–400.
[107] Sonsino C, Maddox S, Haagensen P. A short study on the form of the sn-curves for weld details in the high-cycle-fatigue regime iiw doc; 2005.
[108] Dimitrakis S, Lawrence F. Improving the fatigue performance of fillet weld terminations. Fatigue Fract Eng Mater Struct 2001;24(6):429–38.
[109] Weich I. Ermüdungsverhalten mechanisch nachbehandelter schweißverbindungen in abhängigkeit des randschichtzustands, PhD thesis. Germany: TechnischeUniversität Braunschweig; 2009.
[110] Uchida D, Mori T, Sasaki Y. Influence of grinding depth on fatigue strength of out-of-plane gusset joints with finished weld toes. Kou kouzou rombunshuu 2016;23(89):51–8.
[111] Deguchi T, Mouri M, Hara J, Kano D, Shimoda T, Inamura F, Fukuoka T, Koshio K. Fatigue strength improvement for ship structures by ultrasonic peening. J Mar Sci Technol 2012;17(3):360–9.
[112] Ohta A, Suzuki N, Maeda Y. Shift of S-N curves with stress ratio. Weld World 2003;47(1–2):19–24.
[113] Kawano H, Inoue K, A local approach for fatigue strength evaluation on ship structures. In: Technical research centre of Finland, Fatigue Design 1992, vol. 1; 1992.
[114] Takena K, Kawakami H, Itoh F, Miki C. Stress analysis and calculation of fatigue lives about web-gusset welded joints. Doboku Gakkai Ronbunshu 1988;1988(392):345–50.
[115] Maddox SJ, Doré M, Smith SD. A case study of the use of ultrasonic peening for upgrading a welded steel structure. Weld World 2011;55(9–10):56–67.
[116] Maddox S. Fatigue of steel fillet welds hammer peened under load. Weld World Soudage Monde 1998;41(4):343–9.
[117] Wormsen A, Sjödin B, Härkegard G, Fjeldstad A. Non-local stress approach for fatigue assessment based on weakest-link theory and statistics of extremes. Fatigue Fract Eng Mater Struct 2007;30:1214–27.

[118] Blacha L, Karolczuk A, Banski R, Stasiuk P. Application of the weakest link analysis to the area of fatigue design of steel welded joints. Eng Fail Anal 2013;35:665–77.
[119] Walker K, The effect of stress ratio during crack propagation and fatigue for 2024–t3 and 7075–t6 aluminum. In: Effects of environment and complex load history on fatigue life. ASTM International; 1970.
[120] Taylor D. The theory of critical distances; a new perspective in fracture mechananics. Elsevier; 2007, iSBN: 978-0-08-044478-9.
[121] Baumgartner J, Waterkotte R. Crack initiation and propagation analysis at welds – assessing the total fatigue life of complex structures. Materialwiss Werkstofftech 2015;46(2):123–35. arXiv:https://onlinelibrary.wiley.com/doi/pdf/10.1002/mawe.201400367.
[122] Sonsino C, Hanselka H, Karakas O, Gülsöz A, Voigt M, Dilger K. Fatigue design values for welded joints of the wrought magnesium alloy az31 (iso-mgal3zn1) according to the nominal, structural and notch stress concepts in comparison to welded steel and aluminium connections. Weld World 2013;52:79–94.
[123] Karakas O, Zhang G, Sonsino C. Critical distance approach for the fatigue strength assessment of magnesium welded joints in contrast to neuber's effective stress method. Int J Fatigue 2018;112:21–35.
[124] Duan Z, Shi H, Ma X. Fish-eye shape prediction with gigacycle fatigue failure. Fatigue Fract Eng Mater Struct 2011;34:832–7.
[125] Krasovskyy A, Bachmann D. Estimating the fatigue behavior of welded joints in the vhcf regime. Int J Struct Integrity 2012;3(4):326–43.
[126] Hong Y, Lei Z, Sun C, Zhao A. Propensities of crack interior initiation and early growth for very-high-cycle fatigue of high strength steels. Int J Fatigue 2014;58:144–51.
[127] Mikulski Z, Lassen T. Fatigue crack initiation and subsequent crack growth in fillet welded steel joints. Int J Fatigue 2019;120:303–18.
[128] Zerbst U, Madia M, Schork B. Fracture mechanics based determination of the fatigue strength of weldments. Procedia Struct Integrity 2016;1:010–7.
[129] Zerbst U, Madia M, Vormwald M. Fatigue strength and fracture mechanics. Procedia Struct Integrity 2017;5:745–52.